New Mass and Radius Constraints on the LHS 1140 Planets – LHS 1140 b is Either a Temperate Mini-Neptune or a Water World

```
CHARLES CADIEUX D, MYKHAYLO PLOTNYKOV D, RENÉ DOYON D, MARTIN VALENCIA D, FARBOD JAHANDAR D, LISA DANG D, MARTIN TURBET D, G, THOMAS J. FAUCHEZ D, S, S, 10 RYAN CLOUTIER D, MARTIN CHERUBIM D, 12, 13 ÉTIENNE ARTIGAU D, MARTIN TURBET D, MARTIN TURBET D, MARTIN TURBET D, MARTIN D, MARTIN CHARNAY D, MAR
```

¹ Institut Trottier de recherche sur les exoplanètes, Université de Montréal, 1375 Ave Thérèse-Lavoie-Roux, Montréal, QC, H2V 0B3, Canada

> ²Department of Physics, University of Toronto, Toronto, ON M5S 3H4, Canada ³Observatoire du Mont-Mégantic, Université de Montréal, Montréal H3C 3J7, Canada

⁴Department of Physical & Environmental Sciences, University of Toronto at Scarborough, Toronto, ON M1C 1A4, Canada

⁵David A. Dunlap Dept. of Astronomy & Astrophysics, University of Toronto, 50 St. George Street, Toronto, Ontario, M5S 3H4, Canada

⁶Laboratoire de Météorologie Dynamique/IPSL, CNRS, Sorbonne Université, Ecole Normale Supérieure, PSL Research University, Ecole

Polytechnique, 75005 Paris, France

⁷ Laboratoire d'astrophysique de Bordeaux, Univ. Bordeaux, CNRS, B18N, allée Geoffroy Saint-Hilaire, 33615 Pessac, France
⁸ NASA Goddard Space Flight Center 8800 Greenbelt Road Greenbelt, MD 20771, USA

⁹Integrated Space Science and Technology Institute, Department of Physics, American University, Washington DC

¹⁰NASA GSFC Sellers Exoplanet Environments Collaboration

¹¹Department of Physics & Astronomy, McMaster University, 1280 Main St W, Hamilton, ON, L8S 4L8, Canada
¹²Earth and Planetary Science, Harvard University, 20 Oxford St, Cambridge, MA 02138, USA

¹³ Center for Astrophysics — Harvard & Smithsonian, 60 Garden Street, Cambridge, MA 02138, USA

¹⁴SRON, Netherlands Institute for Space Research, Niels Bohrweg 4, NL-2333 CA, Leiden, The Netherlands

¹⁵Department of Physics and Astronomy, University College London, London, United Kingdom

¹⁶ Department of Physics and Trottier Space Institute, McGill University, Montréal, Québec, H3A 2T8, Canada
¹⁷ LESIA, Observatoire de Paris, Université PSL, CNRS, Sorbonne Université, Université Paris-Cité, 5 place Jules Janssen, 92195
Meudon, France

18 Departement d'astronomie, Université de Genève, Chemin Pegasi, 51, CH-1290 Versoix, Switzerland
 19 Instituto de Astrofísica e Ciências do Espaço, Universidade do Porto, CAUP, Rua das Estrelas, PT4150-762 Porto, Portugal
 20 Departamento de Física e Astronomia, Faculdade de Ciencias, Universidade do Porto, Rua Campo Alegre, 4169-007 Porto, Portugal
 21 Departamento de Física Teórica e Experimental, Universidade Federal do Rio Grande do Norte, Campus Universitário, Natal, RN, 59072-970, Brazil

²² Department of Earth & Planetary Sciences, McGill University, 3450 rue University, Montréal, QC H3A 0E8, Canada
²³ Univ. Grenoble Alpes, CNRS, IPAG, 38000 Grenoble, France

²⁴Instituto de Astrofísica de Canarias, 38205 La Laguna, Tenerife, Spain

 25 Departamento de Astrofísica, Universidad de La Laguna, 38206 La Laguna, Tenerife, Spain

²⁶ European Southern Observatory, Karl-Schwarzschild-Strasse 2, 85748 Garching, Germany

²⁷ Hamburger Sternwarte, Gojenbergsweg 112, 21029 Hamburg, Germany

²⁸ABB, Québec, G1P 0B2, Canada

²⁹ Centre d'optique, photonique et lasers, Université Laval, Québec, G1V 0A6, Canada

Corresponding author: Charles Cadieux charles.cadieux.1@umontreal.ca

³⁰Department of Physics and Space Science, Royal Military College of Canada, PO Box 17000, Station Forces, Kingston, ON, Canada

ABSTRACT

The two-planet transiting system LHS 1140 has been extensively observed since its discovery in 2017, notably with Spitzer, HST, TESS, and ESPRESSO, placing strong constraints on the parameters of the M4.5 host star and its small temperate exoplanets, LHS 1140 b and c. Here, we reanalyse the ESPRESSO observations of LHS 1140 with the novel line-by-line framework designed to fully exploit the radial velocity content of a stellar spectrum while being resilient to outlier measurements. The improved radial velocities, combined with updated stellar parameters, consolidate our knowledge on the mass of LHS 1140 b $(5.60\pm0.19\,\mathrm{M}_{\oplus})$ and LHS 1140 c $(1.91\pm0.06\,\mathrm{M}_{\oplus})$ with unprecedented precision of 3%. Transits from Spitzer, HST, and TESS are jointly analysed for the first time, allowing us to refine the planetary radii of b $(1.730\pm0.025\,\mathrm{R}_{\oplus})$ and c $(1.272\pm0.026\,\mathrm{R}_{\oplus})$. Stellar abundance measurements of refractory elements (Fe, Mg and Si) obtained with NIRPS are used to constrain the internal structure of LHS 1140 b. This planet is unlikely to be a rocky super-Earth as previously reported, but rather a mini-Neptune with a $\sim 0.1\%$ H/He envelope by mass or a water world with a water-mass fraction between 9 and 19% depending on the atmospheric composition and relative abundance of Fe and Mg. While the mini-Neptune case would not be habitable, a water-abundant LHS 1140 b potentially has habitable surface conditions according to 3D global climate models, suggesting liquid water at the substellar point for atmospheres with relatively low CO₂ concentration, from Earth-like to a few bars.

1. INTRODUCTION

The last few years have been fruitful in the quest to uncover exoplanets transiting nearby low-mass stars. Unlike their solar counterparts, M dwarfs represent optimal targets for detailed studies of their planetary systems. They have smaller sizes $(0.1-0.6\,\mathrm{R}_{\odot})$ and masses $(0.1-0.6\,\mathrm{M}_{\odot})$, facilitating the characterization of exoplanets through transit and radial velocity (RV) observations. As they are less luminous, their Habitable Zone (HZ) is more compact than in our solar system, corresponding to orbital periods usually well sampled by current surveys (typically 60 days for an M0, 3 days for an M9). M dwarfs have at least twice as many small exoplanets with $M_{\rm p} \sin i < 10 \,{\rm M}_{\oplus}$ than G-type stars (Sabotta et al. 2021) and make up the majority of systems in the vicinity of the Sun (Revlé et al. 2021, 2022). We thus expect the nearest HZ planets to orbit such kind of stars. This is exemplified with Proxima Centauri (M5.5V), our closest neighbour (1.3 pc; Gaia Collaboration et al. 2021), hosting a nontransiting terrestrial planet in the HZ (Anglada-Escudé et al. 2016; Faria et al. 2022). The M5.5V dwarf GJ 1002 at 4.84 pc also has two non-transiting Earth-mass companions in the HZ recently discovered by Suárez Mascareño et al. (2023). The TRAPPIST-1 system (Gillon et al. 2017) at 12.5 pc has seven terrestrial planets, including three in the HZ, all transiting the M8V ultracool host. These transiting systems are extremely valuable because the radius of exoplanets—sometimes even the mass through transit timing variations as for TRAPPIST-1 (e.g., Agol et al. 2021) — is only accessible via the transit method. Combined with dynamical mass constraints from Doppler spectroscopy, the bulk density

of exoplanets can be obtained, revealing whether their interior is mostly rocky, gaseous, or perhaps even waterrich (Luque & Pallé 2022), but evidence of water worlds remains elusive (Rogers et al. 2023).

The M4.5 dwarf LHS 1140 located at 15.0 pc is another intriguing system, currently the second closest to a transiting HZ exoplanet after TRAPPIST-1. A super-Earth on a 24.7-day temperate orbit was detected in 2017 (Dittmann et al. 2017, hereafter D17) from MEarth photometry (Irwin et al. 2009), followed by the discovery of a second rocky planet with a shorter 3.8-day period (Ment et al. 2019, hereafter M19). The follow-up study of M19 presents a transit visit of LHS 1140 b and c with the Spitzer Space Telescope, largely improving the radius constraints of the two planets. Their masses were derived from HARPS (Pepe et al. 2002) radial velocities, initially for b only by D17, and subsequently for b and c by M19 using an extended data set. This planetary system was revisited in 2020 (Lillo-Box et al. 2020, hereafter LB20) with the ESPRESSO spectrograph (Pepe et al. 2021) and the Transiting Exoplanet Survey Satellite (TESS; Ricker et al. 2015), offering an update of the bulk densities of LHS 1140 b and c, while also hinting at a possible third non-transiting planet on a longer orbit ($P_{\rm d} = 78.9 \,\rm days$). Lastly, transit spectroscopy of LHS 1140 b has been obtained from the ground (Diamond-Lowe et al. 2020) and from space (Edwards et al. 2021) with the Wide Field Camera 3 (WFC3) on the Hubble Space Telescope (HST). Edwards et al. (2021) reported a tentative detection of a hydrogendominated atmosphere with H₂O on LHS 1140b, but the signal (\sim 100 ppm) could also be explained by stellar contamination.

In this letter, we present a new analysis of archival data of LHS 1140 and derive stellar abundances from near-infrared spectroscopy with NIRPS (Bouchy et al. 2017). The ESPRESSO radial velocities were significantly improved using a line-by-line extraction (Artigau et al. 2022) and, for the first time, transit data sets from Spitzer, HST, and TESS were jointly analysed. We describe the observations in Section 2 and characterize the host star in Section 3. We present our revision of the mass and radius of the LHS 1140 planets and discuss their plausible internal structures in Section 4. Concluding remarks follow in Section 5.

2. OBSERVATIONS

2.1. Spitzer photometry

We recovered four *Spitzer* transits of LHS 1140 b taken with the Infrared Array Camera (Fazio et al. 2004) at $4.5\,\mu\mathrm{m}$ from the NASA/IPAC Infrared Science Archive¹. These data include the double transit of LHS 1140 b and c analysed by M19, with three additional unpublished transits of LHS 1140 b (PI: J. A. Dittmann) from the same program. The observations were taken on UT2017-10-02, 2017-10-27, 2018-03-24, and 2018-04-18, hereafter referred to as Transit 1 to 4 (Transit 4 is presented in M19).

The observations were acquired using the subarray mode with a 2s exposure producing datacubes of 64 subarray images of 32×32 pixels. We used the Spitzer Phase Curve Analysis (SPCA) pipeline (Dang et al. 2018; Bell et al. 2021) to extract the photometry and decorrelate against instrumental systematics. For Transits 1 and 3, we use a 3×3 pixel area to extract the target's intensity for each subarray frame. We then median-binned each datacube to mitigate the known subarray instrumental systematics and use Pixel Level Decorrelation (PLD; Deming et al. 2015) to detrend against detector systematics. Similarly to M19, we elect to discard the first 78 minutes of Transit 4 during which the target's centroid had not yet settled on the detector. For Transit 2 and 4, we opted for a different detrending strategy as the shorter baseline before transit tends to bias the retrieved eclipse depth with PLD. Instead, we find that extracting the target photometry with an exact circular aperture with a radius of 3.0 pixels centered on the target's centroid yields the optimal photometric scheme. We then binned each datacube and detrended the instrumental systematics using a 2D polynomial as a function of centroid. The stacked (phase-folded) transit of

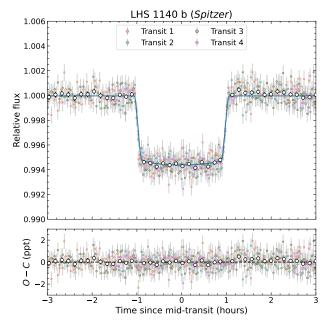


Figure 1. Phase-folded transit of LHS 1140 b observed with *Spitzer* Infrared Array Camera (at $4.5\,\mu\mathrm{m}$). The transit of LHS 1140 c from Transit 4 is masked (see Fig. A1 for individual transits). The open circles represent 8-minute binned photometry and the blue curve depicts the best-fit transit model. The residuals of this fit are shown below.

LHS 1140 b is presented in Figure 1. The individual detrended transits are presented Figure A1.

2.2. HST WFC3 white light curve

Two transits of LHS 1140 b were observed with HST WFC3 on UT2017-01-28 and UT2017-12-15 (PN: 14888; PI: J. A. Dittmann). Unfortunately, due to large shifts in the position of the spectrum on the detector, the observation from UT2017-01-28 could not be reliably analysed (Edwards et al. 2021). The transit on UT2017-12-15 was successfully analysed by Edwards et al. (2021) to constrain the transmission spectrum of LHS 1140 b near $1.4 \,\mu\text{m}$. The observations were conducted in the G141 grism configuration with the GRISM256 aperture (256×256 subarray) and 103.13 s integration time. Readers are referred to Edwards et al. (2021) for a complete description of the HST data reduction that made use of the Iraclis software (Tsiaras et al. 2016). Here, we include the extracted white light curve from HST (Fig. A2) for our transit analysis.

2.3. TESS photometry

LHS 1140 (TIC 92226327, TOI-256) was observed with TESS at a 2-minute cadence during its primary mission from September 20 to October 17, 2018 (Sector 3) and during its first extended mission from September 23 to October 20, 2020 (Sector 30). We used the Presearch Data Conditioning Simple Aperture Photometry

¹ irsa.ipac.caltech.edu/

(PDCSAP; Smith et al. 2012; Stumpe et al. 2012, 2014) data product issued by the TESS Science Processing Operations Center (SPOC, Jenkins et al. 2016) at NASA Ames Research Center and available on the Mikulski Archive for Space Telescopes². The PDCSAP data includes corrections for instrumental systematics and for flux dilution from known Gaia sources within several TESS pixels (21" per pixel). The light curve from Sector 3 was reprocessed with a more recent release of SPOC (version 5.0.20), which applies the new background correction implemented for the extended mission to the first sectors of TESS. This new correction typically reduces the inferred transit depths by less than 2%. Using the same pipeline (SPOC v5.0) for Sectors 3 and 30 ensures consistent transit depths for LHS 1140 b and c between primary and extended mission data. The full TESS light curve of LHS 1140 shown in Figure A3 captures 2 and 11 transits of planet b and c, respectively, twice as many as in LB20 based on Sector 3 data only. The phasefolded transits from TESS are also shown in the same Figure A3.

2.4. ESPRESSO radial velocity

We retrieved publicly available ESPRESSO data of LHS 1140 from the European Southern Observatory (ESO) science archive³ (Delmotte et al. 2006). These data consist of the same 117 spectra analysed in LB20 and taken with the SINGLEHR21 mode between October 2018 and December 2019. We used the bias & dark subtracted, extracted and flat-fielded spectra reduced with the ESPRESSO pipeline (version 2.2.1)⁴. The RV extraction from the reduced data was performed with the line-by-line (LBL, version 0.52) method of Artigau et al. (2022) available as an open source package⁵. A simple telluric correction is first performed inside the LBL code by fitting a TAPAS (Bertaux et al. 2014) atmospheric model. This correction step, comparable to the approach of Allart et al. (2022), has been demonstrated to improve the RV precision of ESPRESSO particularly for M-type stars.

At the core of the LBL method, first explored by Dumusque (2018), Doppler shifts are measured on the smallest spectral range possible, i.e., a spectral line, from a high signal-to-noise ratio (SNR) template spectrum of the star and its first derivative (Bouchy et al. 2001). This template is constructed by coadding all our 117 telluric-corrected spectra. Then, the statistical

consistency between all per-line velocities (~38 000 for LHS 1140) is verified using a simple mixture model (Appendix B of Artigau et al. 2022) that effectively remove high-sigma outliers to produce a final error-weighted average of valid lines. This approach fully exploits the RV content of a stellar spectrum and is conceptually similar to widely employed template-matching algorithms (e.g., Anglada-Escudé & Butler 2012, Astudillo-Defru et al. 2017, Zechmeister et al. 2018, Silva et al. 2022) while being more resilient to outlying spectral features (e.g., telluric residuals, cosmic rays, detector defects).

Following LB20, we separately analysed the data taken before and after the fiber link change of ESPRESSO in June 2019 (Pepe et al. 2021), hereafter designated as "pre" and "post" velocities. Using an iterative sigma-clipping algorithm, we removed two epochs (BJD = 2458703.787210 and 2458766.704332) flaggedas $>3\sigma$ outliers. The final radial velocities are given in Table B1 and show a median uncertainty of $0.36\,\mathrm{m\,s^{-1}}$ and dispersion (RMS) of $4.07 \,\mathrm{m\,s^{-1}}$. As a comparison, the published values of LB20 derived from the crosscorrelation function (CCF) technique have a median precision of $0.99 \,\mathrm{m \, s^{-1}}$, almost three times larger than LBL, and a 4.76 m s⁻¹ scatter. Figure 2 presents a comparison between LBL and CCF for the best-fit orbits of LHS 1140 b and c. The full LBL RV sequence is shown in Figure B1. Given the extreme precision of ESPRESSO with LBL, a joint analysis with the HARPS data also available through the ESO archive has resulted in identical semi-amplitudes for LHS 1140 b and c. For this reason and to simplify the analysis, we opted to only use ESPRESSO in this work. The ESPRESSO observations span approximately 400 days, a long enough baseline to characterize signals at longer periods, such as the candidate LHS 1140 d ($P_{\rm d}=78.9\,{\rm days}$) or the rotation of the star ($P_{\text{rot}} = 131 \,\text{days}; \,\text{D17}$). As discussed in Appendices D.1 and D.3, we find no evidence for LHS 1140 d and attribute this 80-day signal most likely to stellar activity.

2.5. NIRPS high-resolution spectroscopy

We acquired 29 high-resolution spectra of LHS 1140 with the Near-InfraRed Planet Searcher (NIRPS; Bouchy et al. 2017; Wildi et al. 2022) during one of its commissioning phases (Prog-ID 60.A-9109) from 2022-11-26 to 2022-12-06. NIRPS is a new echelle spectrograph designed for precision RV at the ESO 3.6-m telescope in La Silla, Chile covering the YJH bands (980–1800 nm). The instrument is equipped with a high-order Adaptive Optics (AO) system and two observing modes, High Accuracy (HA, $R \approx 85\,000,\ 0.4''$ fiber) and High Efficiency (HE, $R \approx 70\,000,\ 0.9''$ fiber), that can both

² archive.stsci.edu/tess/

³ archive.eso.org/

⁴ eso.org/sci/software/pipelines/espresso/

⁵ github.com/njcuk9999/1bl

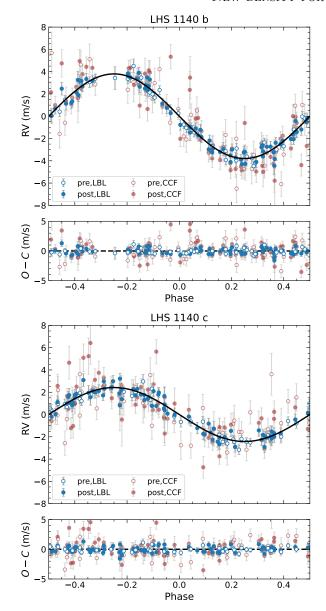


Figure 2. Phase-folded Keplerian signals of LHS 1140 b (top) and c (bottom) with ESPRESSO from RVs produced with the line-by-line (LBL) method in blue and from cross-correlation function (CCF) in red (Lillo-Box et al. 2020). Open and solid data points represent pre- and post-fiber upgrade of ESPRESSO (June 2019). The best-fit circular orbital solutions (black curves) of LHS 1140 b ($K_b = 3.80 \pm 0.11 \,\mathrm{m\,s^{-1}}$) and c ($K_c = 2.42 \pm 0.07 \,\mathrm{m\,s^{-1}}$) are respectively improved by 50% and 70% compared with previous estimates with CCF. The residuals RMS is equivalent to $0.50 \,\mathrm{m\,s^{-1}}$ for LBL and $1.28 \,\mathrm{m\,s^{-1}}$ for CCF.

be utilized simultaneously with HARPS. LHS 1140 was observed in HE mode as an RV standard star to test the stability of the instrument preceding the official start of NIRPS operation in April 2023. The observations were reduced with APERO v0.7.271 (Cook et al. 2022), the standard data reduction software for the SPIRou near-

infrared spectrograph (Donati et al. 2020), fully compatible with NIRPS. We built a template spectrum of LHS 1140 from the telluric-corrected data product from APERO to derive independent stellar parameters and the abundances of several elements (Sect. 3.2). This template spectrum combines 29 individual spectra each with a SNR per pixel of about 70 in the middle of H band.

3. STELLAR CHARACTERIZATION

The star LHS 1140 was characterized in previous studies (D17; M19; LB20). In this section, we summarize our work to revise the stellar mass and radius and to measure the effective temperature and stellar abundances with NIRPS. An analysis of the stellar kinematics confirming the age ($>5\,\mathrm{Gyr},\ \mathrm{D17}$) and galactic thin disk membership of LHS 1140 is presented in Appendix C.1.

3.1. Stellar mass and radius update

We pulled the K_s magnitude (8.82 \pm 0.02) of LHS 1140 from 2MASS (Skrutskie et al. 2006) and its distance d from Gaia DR3 ($14.96\pm0.01\,\mathrm{pc}$; Gaia Collaboration et al. 2021). Then, from the absolute K_s magnitude $(M_{K_{\bullet}})$ to M_{\star} empirical relation of Mann et al. (2019), we obtain a stellar mass of $0.1844 \pm 0.0046 \,\mathrm{M}_{\odot}$, with uncertainty propagating the errors on K_s , d, and the scatter of this relation. This revised and more precise stellar mass is consistent with that of M19 ($M_{\star} = 0.179 \pm 0.014 \,\mathrm{M}_{\odot}$) obtained from a similar mass-luminosity calibration (Benedict et al. 2016), but using a smaller sample of nearby binaries. In a similar way, but using the M_{K_s} - R_{\star} relationship of Mann et al. (2015), we obtain a radius of $0.2153 \pm 0.0065 \,\mathrm{R}_{\odot}$ for LHS 1140. M19 determine the stellar radius from an analysis of the transits, yielding a slightly more precise $R_{\star} = 0.2139 \pm 0.0041 \,\mathrm{R}_{\odot}$. To make sure that our results are completely independent of previous analyses, we first adopt the value derived from Mann et al. (2015) as a prior, then further constrained the radius from the stellar density inferred from transits. This Bayesian method is detailed in Appendix C.2 and results in a new stellar mass and radius of M_{\star} = $0.1844 \pm 0.0045 \,\mathrm{R}_{\odot}$ and $R_{\star} = 0.2159 \pm 0.0030 \,\mathrm{R}_{\odot}$. The stellar parameters of LHS 1140 are listed in Table C1.

3.2. Stellar abundances from NIRPS

We follow the methodology of Jahandar et al. (2023), also applied in Cadieux et al. (2022) for TOI-1452 (M4) and in Gan et al. (2023) for TOI-4201 (M0.5), to derive the effective temperature as well as the abundances of several chemical species in LHS 1140 from the NIRPS template spectrum. A global fit (χ^2 minimization) to a selection of strong spectral lines using ACES stellar models (Allard et al. 2012; Husser et al. 2013) convolved

to match NIRPS resolution resulted in a $T_{\rm eff}=3096\pm48\,{\rm K}$ and a [M/H] = 0.01 ± 0.04 for LHS 1140. Note we fixed log g=5 (cgs) for our grid of models in accordance to LHS 1140 (Table C1). This method was empirically calibrated for log g of $5.0\pm0.2\,{\rm dex}$ (Jahandar et al. 2023).

We then performed a series of fits for a fixed $T_{\rm eff} =$ 3100 K on individual spectral lines of known chemical species to derive their elemental abundances (again following Jahandar et al. 2023). We show an example of this method in Figure C2 for the Al I line at 1675.514 nm from which we measure $[Al/H] = 0.0 \pm 0.1 \, dex$ from this single line. The average abundances for all chemical species detected in LHS 1140 are given in Table C2 including the refractory elements Fe, Mg, and Si that form the bulk material of planetary cores and mantles. As shown in Table C3, LHS 1140 features a relatively low Fe/Mg weight ratio $(1.03^{+0.40}_{-0.29})$ compared to the Sun (1.87 ± 0.22) and other solar neighbourhood M dwarfs, with a C/O measurement consistent with the solar value. The measured Fe/Mg abundance ratio is used later as input to planetary internal structure models (Sect. 4.2).

4. RESULTS & DISCUSSION

4.1. New density measurements

We measure the physical and orbital parameters of LHS 1140 b and c by jointly fitting transit and Keplerian models to the photometric (*Spitzer*, HST, and TESS) and RV (ESPRESSO) observations. The details of this joint transit RV fit are presented in Appendix D.1. Notably, the best-fit solution is two planets on circular orbits (Table D1) with no evidence of candidate LHS 1140 d. We adopt the average radius measured by *Spitzer* and TESS for LHS 1140 c but discuss an important discrepancy between the two measurements in Appendix D.2.

We infer a mass of $5.60\pm0.19\,\mathrm{M}_{\oplus}$ for LHS 1140 b and $1.91\pm0.06\,\mathrm{M}_{\oplus}$ for LHS 1140 c, as well as planetary radii of $1.730\pm0.025\,\mathrm{R}_{\oplus}$ for b and $1.272\pm0.026\,\mathrm{R}_{\oplus}$ for c. The LHS 1140 planets are among the best-characterized exoplanets to date, with relative uncertainties of only 3% for the mass and 2% for the radius, reaching a similar precision to the TRAPPIST-1 planets (Agol et al. 2021). These measurements correspond to bulk densities of 5.9 ± 0.3 g cm⁻³ and 5.1 ± 0.4 g cm⁻³ for planet b and c, respectively. The results of previous studies for the semi-amplitudes (K) and scaled radii (R_p/R_*) of the planets are shown in Table 1. Since LB20, our updated $R_{\rm p}/R_{\star}$ ratios have increased back to M19 values. This change results from incorporating additional transits with Spitzer and HST, as we retrieve the same $R_{\rm p}/R_{\star}$ as LB20 to 1σ when fitting the TESS data only (see Fig. D1). Note our revision of the mass and radius

Table 1. Comparison of the semi-amplitudes and scaled radii of the LHS 1140 planets from different studies

Parameter	D17	M19	LB20	This work
LHS 1140 b				
$K ({\rm m s^{-1}})$	$5.34{\pm}1.10$	$4.85{\pm}0.55$	$4.21 {\pm} 0.24$	$3.80 {\pm} 0.11$
$R_{\rm p}/R_{\star}~(\%)$	7.08 ± 0.13	7.39 ± 0.01	7.02 ± 0.19	7.33 ± 0.04
LHS 1140 c				
$K ({\rm m s^{-1}})$		$2.35{\pm}0.49$	$2.22{\pm}0.20$	$2.42{\pm}0.07$
$R_{\rm p}/R_{\star}~(\%)$	_	$5.49 {\pm} 0.01$	$5.02 {\pm} 0.16$	$5.39 {\pm} 0.08$

NOTE—D17 with MEarth and HARPS. M19 with MEarth (extended), *Spitzer* and HARPS (extended). LB20 with TESS, HARPS (M19), and ESPRESSO. This work with *Spitzer* (extended), HST, TESS (extended), and ESPRESSO (LB20).

of LHS 1140 b and c is dominated (by more than 80%) by K and $R_{\rm p}/R_{\star}$ changes, not by the update of stellar parameters.

We compare our updated mass and radius to the M dwarf exoplanet population in Figure 3 with various pure composition curves included in the same figure. A detailed analysis of the internal structure of LHS 1140 b is presented in Section 4.2. First examining LHS 1140 b in Figure 3, we see that our revised mass and radius are off the Earth-like track, contradicting previous results from M19 and LB20 that this planet is a rocky, larger version of Earth (super-Earth). The mode of the distribution lies above the pure Mg-Si rock sequence, a region of the mass-radius diagram requiring an additional input of light elements, i.e., gas (H₂, He) or ices (e.g., H₂O, CH₄, NH₃), to explain the observed radius. LHS 1140 b is on the lower limit of the synthetic sub-Neptune population around M dwarfs of Rogers et al. 2023 (orange region in Fig. 3) that have undergone thermal evolution and atmospheric mass loss (photoevaporation) over 5 Gyr assuming initial H/He mass fraction between 0.1% and 30%. With a small $T_{\rm eq}$ of 226 K, Rogers et al. 2023 predict a $\sim 0.1\%$ H/He mass fraction for LHS 1140 b which we confirm through simulation in Section 4.2.1. Alternatively, the planet could be purely rocky or with a water-mass fraction of 10–20%, clearly not as high as the water-rich (50% H₂O) population suggested by Luque & Pallé (2022). Note this latter scenario would involve a different formation mechanism, as suggested by recent studies (Cloutier & Menou 2020; Luque & Pallé 2022; Piaulet et al. 2023; Cherubim et al. 2023), where small planets around M dwarfs could directly accrete icy materials outside the water snow line before migrating inwards, in which case sub-Neptunes would actually be water worlds rather than H/He-enveloped planets.

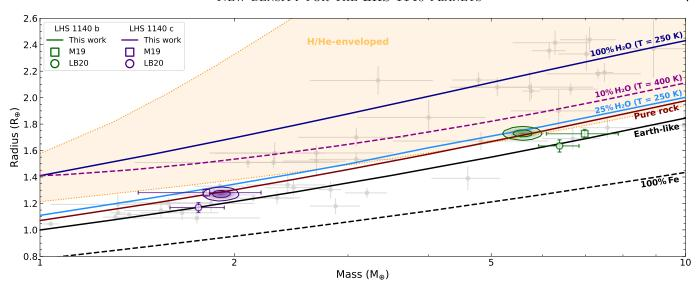


Figure 3. Mass-radius diagram of transiting exoplanets around M dwarfs (gray points) with well-established mass and radius (relative uncertainty < 30%) from the NASA Exoplanet Archive (Akeson et al. 2013). Various theoretical composition curves from Guillot & Morel (1995); Valencia et al. (2007, 2013); Aguichine et al. (2021) are plotted with the water-rich models assuming an Earth-like interior (33% iron by mass). The synthetic population of terrestrials enveloped in H/He (0.1–30% initial mass fraction) of Rogers et al. 2023 is highlighted in orange. This region also highlights interior model degeneracy where the nature (H/He-rich or water-rich) of sub-Neptunes cannot be reliably determined from mass and radius alone. The mass and radius posteriors (1- and 2- σ contours) of LHS 1140 b (green) and LHS 1140 c (purple) from our joint transit RV analysis are drawn. Published values from Lillo-Box et al. 2020 (LB20) derived from HARPS+ESPRESSO and TESS (Sector 3) are shown with open circles. The results of Ment et al. 2019 (M19) from HARPS and MEarth+Spitzer are presented with open squares.

For LHS 1140 c, our mass measurement agrees with previous studies, but we show in Appendix D.2 that Spitzer and TESS radii are in 4σ disagreement, complicating the determination of its internal structure. In Figure 3, we present the average Spitzer+TESS radius of LHS 1140 c most compatible with a rocky interior depleted in iron relative to Earth, but should the planet be smaller, as measured by TESS, an Earth-like interior remains plausible. However, given the planet size and higher $T_{\rm eq}$ of 422 K, a hydrogen-dominated atmosphere or an important water content ($\gtrsim 10\%$ by mass) similar to LHS 1140 b are formally rejected.

4.2. Nature of LHS 1140 b

The unprecedented precisions of both the mass and radius of the LHS 1140 planets combined with stellar abundance measurements provide a unique opportunity to better constrain the nature of these planets. Because of the radius uncertainty associated with LHS 1140 c discussed above, we focus our analysis on LHS 1140 b. The mass—radius diagram of Figure 3 suggests three potential scenarios: (1) a mini-Neptune depleted in hydrogen, (2) a pure rocky (and airless) planet and (3) a water world. All three possibilities are discussed below.

To address scenarios 2 and 3, we follow the method of Plotnykov & Valencia (2020) also applied to the waterworld candidate TOI-1452 b (Cadieux et al. 2022) to constrain both the core-mass fraction (CMF) and watermass fraction (WMF) of the planet. The adaptation of this method to LHS 1140 b is further detailed in Appendix E.1 with the posterior distributions available in Appendix E.2. In brief, this interior analysis treats the Fe/Mg ratio either as a free output parameter completely constrained by the mass-radius data (the no prior case) or as direct input informed by the measured stellar value (the stellar prior case) with Fe/Mg_{planet} $\sim \mathcal{N}(\text{Fe/Mg}_{\text{star}}, \sigma_{\text{star}}^2)$. This latter case assumes that stellar abundances are a good proxy of planetary abundances as suggested by planet formation studies (e.g., Bond et al. 2010, Thiabaud et al. 2015, Unterborn et al. 2016) and empirically (e.g., Dorn et al. 2017, Bonsor et al. 2021) though this correlation is not necessarily 1:1 (Adibekyan et al. 2021).

4.2.1. Hydrogen-poor mini-Neptune

An Earth-like interior (CMF = 33%, WMF \sim 0) overlain by a solar mixture of hydrogen-helium contributing \sim 0.1% of the mass, \sim 10% of the radius could explain the density of LHS 1140 b. Here, we simulate the photoevaporation history of LHS 1140 b for 10 Gyr using the method of Cherubim et al. (2023) to verify whether such hydrogen-rich envelope could survive at present day. These simulations take into account thermal evolution, photoevaporation (e.g., Owen & Wu 2017) from stellar extreme ultraviolet (XUV; 10–130 nm) and corepowered atmospheric escape (e.g., Ginzburg et al. 2018).

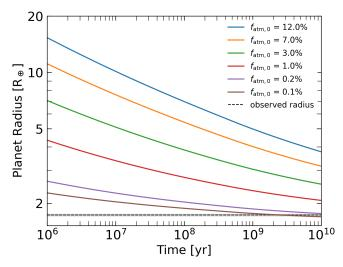


Figure 4. Primordial H/He atmosphere photoevaporation simulation of LHS 1140 b. Each curve corresponds to different initial envelope mass fractions $f_{\rm atm,0}$. These simulations model thermal contraction, XUV-driven atmospheric escape, and core-powered mass loss using the methodology of Cherubim et al. (2023). A $f_{\rm atm,0} = 0.1$ –0.2% is consistent with the observed radius given the age of the system (>5 Gyr).

The results for a range of initial envelope mass fractions ($f_{\text{atm},0}$ between 0.1% and 12%) are shown in Figure 4. Assuming that LHS 1140 b did not undergo important migration after formation, it appears that a $f_{\rm atm,0} = 0.1 - 0.2\%$ (brown and purple curves in Fig. 4) is in agreement with the observed radius after 5 Gyr, the minimum age estimate of the system. Since gas accretion models typically predict initial envelopes with mass fractions $\gtrsim 1\%$ (Ginzburg et al. 2016), such a small $f_{\rm atm,0}$ for LHS 1140 b would imply a formation in a gaspoor environment in less than 0.1 Myr (Lee & Connors 2021) or that it lost part of its atmosphere during giant impacts (Inamdar & Schlichting 2016). The relatively large semi-major axis of LHS 1140 b ($\sim 0.1 \,\mathrm{au}$) is just beyond the instellation needed to strip the atmosphere: the final f_{atm} after 10 Gyr is close to the initial $f_{\text{atm},0}$. In other words, the radius evolution over the simulation timescale is dominated by the cooling/contraction of the atmosphere.

4.2.2. Pure rocky planet

This is the special case of a rocky planet with no water envelope, i.e., the WMF forced to zero. With no prior on the Fe/Mg ratio, our model converges to a very small CMF $(4.3^{+4.1}_{-2.7}\%)$ essentially consistent with a coreless planet with a predicted Fe/Mg ratio $(0.37^{+0.12}_{-0.07})$ significantly lower (2.3σ) than observed for the host star $(1.03^{+0.40}_{-0.29})$ and much smaller than the lowest value ever measured in M dwarfs of the solar neighbourhood (see Fig. E1). Moreover, this model converges to a larger

mass and smaller radius than observed (2.3σ) offset in density). We argue that the inconsistency with the observations coupled with the challenge of forming highly iron depleted (coreless) planets (Carter et al. 2015; Scora et al. 2020; Spaargaren et al. 2023) make this scenario implausible for LHS 1140 b. This conclusion is in line with exoplanet demographics (Rogers 2015) and the empirical rocky-to-gaseous transition around M dwarfs (Cloutier & Menou 2020) that most $\sim 1.6 \, \mathrm{R}_{\oplus}$ exoplanets are not rocky.

4.2.3. Water world

For this scenario, we also include an atmospheric layer, essentially a (small) fixed radius correction associated with a potential atmosphere. For the general case of a water world receiving more irradiation than the runaway greenhouse threshold ($T_{\rm eq} \gtrsim 300 \, {\rm K}$; Turbet et al. 2020; Aguichine et al. 2021), the outer layer is likely to be supercritical, which would significantly inflate the radius, requiring a proper joint modeling of the warm water layer in vapor/supercritical state on top of a core+mantle interior. While we defer this general case to a future publication (Plotnykov et al. in prep.), LHS 1140 b with a small $T_{\rm eq} = 226 \pm 6 \,\mathrm{K}$ does not warrant such a detailed treatment since a potential outer water layer on this planet is most likely to be either in frozen or liquid state as the planet resides in the Water Condensation Zone (Turbet et al. 2023). We thus assume the atmospheric layer of LHS 1140 b to be an Earth-like atmosphere with a surface pressure of 1 bar and surface temperature equal to $T_{\rm eq}$. The radius correction (a few tens of kilometers) for such a thin atmosphere is negligible.

Two prior cases for the Fe/Mg abundance ratio are considered. The unconstrained case (no prior) yields $\mathrm{CMF} = 28.3^{+14.3}_{-15.9}\%$ and a WMF = $18.7^{+12.6}_{-9.8}\%$ while assuming that the planet shares the same Fe/Mg ratio as the host star (stellar prior), we obtain $\mathrm{CMF} = 20.5^{+5.5}_{-5.8}\%$ and WMF = $13.7^{+5.4}_{-4.5}\%$. As shown in Table 2, adopting a solar Fe/Mg ratio instead of those measured on LHS 1140 yields an even larger WMF. We tested changing the surface temperature and pressure (using climate predictions from Sect. 4.3) to generate fully solid/liquid water surface. The effect of phase change is small: both CMF and WMF remained within the reported uncertainty for all models.

A variant of this model is the Hycean world (Madhusudhan et al. 2021), i.e., a water world surrounded by a thin H/He-rich layer as was recently proposed for the temperate mini-Neptune K2-18b (Madhusudhan et al. 2023). This new result opens the possibility that LHS 1140b may be a lower-mass version of such a

Table 2. Summary of the interior models of LHS 1140 b

Model	CMF (%)	WMF (%)	Fe/Mg [w]
LHS 1140			
Host star (reference)	_	-	$1.0^{+0.4}_{-0.3}$
LHS 1140 b			
Purely rocky (no prior)	$4.3_{-2.7}^{+4.2}$	-	$0.4^{+0.1}_{-0.1}$
Water world (no prior)	$28.3^{+14.3}_{-15.9}$	$18.7^{+12.6}_{-9.8}$	$1.6^{+2.5}_{-0.9}$
Water world (stellar prior)	$20.5^{+5.5}_{-5.8}$	$13.7^{+5.4}_{-4.5}$	$1.1^{+0.3}_{-0.3}$
Water world (solar prior)	$27.8^{+4.6}_{-4.2}$	$17.1^{+5.2}_{-5.0}$	$1.8^{+0.2}_{-0.2}$
Hycean world* (stellar prior)	$21.7^{+5.4}_{-6.6}$	$9.3^{+4.6}_{-3.9}$	$1.1^{+0.3}_{-0.3}$

NOTE—*The Hycean model is derived from the Water world model (stellar prior) by subtracting 250 km to the planetary radius corresponding to 5 atmospheric scale heights of H₂.

Hycean planet in the middle of the radius valley (Fulton et al. 2017). In this scenario, the lower mean molecular weight of the atmosphere yields a higher radius correction (up to 250 km for $\mu \sim 2$) corresponding to $\sim 2\%$ of the planet radius. This case with stellar prior on Fe/Mg still yields a significant WMF = $9.3^{+4.6}_{-3.9}\%$ with CMF = $21.7^{+5.4}_{-6.6}\%$.

The main conclusion from this modeling exercise summarized in Table 2 is that LHS 1140 b is unlikely to be a rocky super-Earth. The planet is either a unique mini-Neptune with a thin $\sim 0.1\%$ H/He atmosphere or a water world with a WMF in the 9–19% range depending on the atmospheric composition and the Fe/Mg ratio of the planetary interior. Transmission spectroscopic observations with JWST (Gardner et al. 2023) will be key to discriminate between these scenarios.

4.3. 3D GCM of LHS 1140 b and prospects for atmospheric characterization

Here we consider the case of a water world with a thin atmosphere for LHS 1140 b as this scenario presents broader implications for habitability. Planets with large amounts of water are likely to have $CO_2+N_2+H_2O$ atmospheres (Forget & Leconte 2014; Kite & Ford 2018), possibly with high amounts of CO_2 (Marounina & Rogers 2020). While the diversity of water-world atmospheres has yet to be explored, we adopt here two distinct atmospheric compositions as a first working hypothesis and proof of concept to predict the transmission spectrum of LHS 1140 b: an Earth-like atmosphere (1 bar N_2 , 400 ppm CO_2) and a CO_2 -dominated atmosphere (5 bar CO_2).

The simulations were computed with the Generic Planetary Climate Model (hereafter simply called

state-of-the-art 3DGCM). a climate model (Wordsworth et al. 2011) historically known as the LMD (Laboratoire de Météorologie Dynamique, Paris, France) Generic Global Climate Model. The model has been widely applied to simulate all types of exoplanets, ranging from terrestrial planets like the TRAPPIST-1 planets (Turbet et al. 2018; Fauchez et al. 2019) to mini-Neptunes like GJ 1214 b (Charnay et al. 2015) or K2-18b (Charnay et al. 2021). The GCM uses an upto-date generalized radiative transfer and can simulate a wide range of atmospheric compositions (N2, H2O, CO_2 , etc.) including clouds self-consistently.

The model was used to make realistic predictions of LHS 1140 b's atmospheric properties (temperature–pressure profile, water vapor, and cloud mixing ratios), summarized in Figure 5. We find that no matter how much CO₂ is included in the model, the planet has a patch of liquid water at the substellar point. The extent of the ice-free ocean grows with increasing atmospheric CO₂, due to the greenhouse effect. This result is similar to that shown by Turbet et al. (2016); Boutle et al. (2017); Del Genio et al. (2018) for Proxima b and Wolf et al. (2017); Turbet et al. (2018); Fauchez et al. (2019) for TRAPPIST-1 planets, that water worlds synchronously rotating in the Habitable Zone of low-mass stars almost always have surface liquid water, at least at the substellar point.

Note that the GCM simulations presented here do not include dynamic ocean and sea ice transport, which could slightly change the extent of the substellar liquid water ocean depending on the amount of $\rm CO_2$ (Del Genio et al. 2019; Yang et al. 2020). Note also that we assumed that LHS 1140 b is in synchronous rotation. This is the most likely rotation mode given LHS 1140 b's proximity to its star and low eccentricity (Ribas et al. 2016), producing gravitational tides which are expected to dominate atmospheric tides for this planet (Leconte et al. 2015).

The outputs of the GCM were used to compute realistic transmission spectra that take into account the 3D nature of the atmosphere. We used the Planetary Spectrum Generator (PSG; Villanueva et al. 2018, 2022) to produce transmission spectrum models (following the methodology of Fauchez et al. 2019) of LHS 1140 b based on the output of the two GCM simulations including the effects of $\rm H_2O/CO_2$ clouds. As shown in Figure 6, the strongest atmospheric feature predicted by these models is $\rm CO_2$ near $4.3\,\mu{\rm m}$ with a strength of about 15 ppm. Changing the partial pressure of $\rm CO_2$ from 400 ppm to 5 bars produces a similar $\rm CO_2$ bump as this molecule essentially condenses at higher concentration to form ice particles at low altitude (see Fig. 5, panel h).

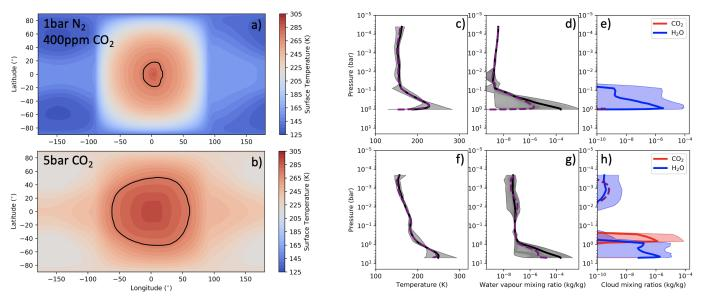


Figure 5. Results of Global Climate Model (GCM) simulations of LHS 1140 b assuming an Earth-like atmosphere (1 bar N₂, 400 ppm CO₂; panels a, c, d, e) and a thick CO₂-dominated atmosphere (5 bar CO₂; panels b, f, g, h). *Panels a, b*: Surface temperature maps of LHS 1140 b. The black line indicates the line of stability between liquid water and sea ice. The extent of the ice-free ocean strongly depends on the amount of CO₂ in the atmosphere. *Panels c, d, e, f, g, and h*: Vertical profiles of the atmospheric temperatures, water vapor, and cloud mixing ratios (both H₂O and CO₂ ice clouds). The solid bold lines indicate the global mean vertical profiles and the dotted lines indicate terminator vertical profiles (impacting transit spectra).

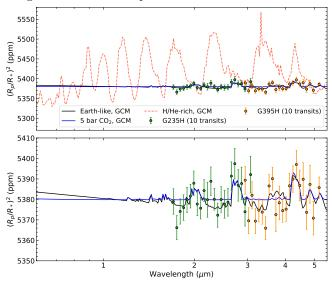


Figure 6. Predicted transmission spectrum of LHS 1140 b from 0.6 to $5.5\,\mu\mathrm{m}$ for the Earth-like (black) and 5 bar CO₂ (blue) global climate models (GCM, Fig. 5). The bottom panel is a zoom of the top panel. Simulated JWST/NIRSpec data with the G235H (green) and G395H (orange) dispersers are shown. We estimate that 20 transits equally divided between G235H and G395H are required to detect a secondary atmosphere around LHS 1140 b at 4σ . The red dashed curve is a GCM-based representation of a mini-Neptune (H/Herich) that can be easily detected with a single visit.

LHS 1140 b was observed twice in transit with JWST in July 2023 during Cycle 1 (PID: 2334, PI: M. Damiano,

unpublished). The two visits were made with NIRSpec (Böker et al. 2023) using the Bright Object Time Series mode, one transit with the G235H disperser (1.66– $3.05 \,\mu\text{m}$) and the other with G395H (2.87–5.14 μm). We used PandExo (Batalha et al. 2017) to simulate NIR-Spec observations, keeping the same observing strategy of alternating between G235H and G395H. For a degraded spectral resolution of $R \simeq 20$ and assuming a conservative 5 ppm noise floor (Coulombe et al. 2023), these simulations predict sensitivity of about 20 ppm for G235H/G395H per spectral bin and per transit. As shown in Figure 6, the Cycle 1 data has the capability to identify the mini-Neptune scenario, but should LHS 1140b be a water world, we predict that an additional 18 transits (20 in total) would be required to detect its atmosphere (at 4σ). This estimation is made by simulating 1000 transmission spectra and comparing the log Bayesian evidence $(\ln Z)$ between a flat spectrum and the Earth-like model of Figure 6 with the median simulation shown in the same figure yielding a $\Delta \ln Z = 6.5$ or 4σ (Benneke & Seager 2013). Note, the optimal observing strategy has yet to be fine-tuned depending on the level of stellar contamination yet to be characterized. This may warrant some visits to be obtained regularly with NIRISS SOSS (0.6–2.8 μ m; Doyon et al. 2023, Albert et al. 2023).

It should be noted that only four transits are observable every year with JWST as a result of the 24.7-day

period of LHS 1140 b and the fact that the system is near the ecliptic. An in-depth atmospheric characterization will realistically require that all future transit events of this planet be observed with JWST over several years (at least 3 years to detect a 15 ppm CO₂ signal at 3σ). Irrespective of the nature of LHS 1140 b, we advocate initiating an extensive campaign as soon as possible considering the uniqueness of this temperate world.

5. SUMMARY & CONCLUSION

In this letter, we revisited the M4.5 LHS 1140 system hosting two transiting small exoplanets including LHS 1140 b in the Habitable Zone. We applied the novel line-by-line precision radial velocity method of Artigau et al. (2022) to publicly available ESPRESSO data, previously analysed by Lillo-Box et al. (2020) using the cross-correlation function technique. The improvement on the radial velocities is significant: the errors are reduced by almost a factor three, the residual dispersion is halved, and no important excess white noise is detected. By jointly fitting the RVs with transits from Spitzer (3 new archival transits), HST, and TESS (new Sector 30), we update the planetary mass and radius to $5.60\pm0.19\,\mathrm{M}_{\oplus}$ and $1.730\pm0.025\,\mathrm{R}_{\oplus}$ for LHS 1140 b, $1.91\pm0.06\,\mathrm{M}_{\oplus}$ and $1.272\pm0.026\,\mathrm{R}_{\oplus}$ for LHS 1140 c. The improved radial velocity data do not support the existence of the non-transiting candidate LHS 1140 d announced by Lillo-Box et al. (2020).

Our revised mass and radius measurements reveal that LHS 1140b is unlikely to be a rocky super-Earth as previously reported, as it would require: (1) A density larger (by 2.3σ) than observed, (2) A core-mass fraction consistent with a coreless planet (CMF = $4.3^{+4.2}_{-2.7}\%$), (3) A planetary Fe/Mg weight ratio smaller (2.3σ) than measured on its host star and never measured in any solar neighbourhood M dwarfs. Instead, our analysis shows that LHS 1140 b could either be one of the smallest known mini-Neptune ($\sim 0.1\%$ H/He by mass) with an atmosphere stable to mass loss over the lifetime of the system or a water world with a significant watermass fraction of $13.7^{+5.5}_{-4.5}\%$ when the iron-to-magnesium weight ratio of the planet is informed by those measured with NIRPS on the host star (Fe/Mg = $1.03^{+0.40}_{-0.29}$). For LHS 1140 c, our updated density is consistent with a rocky world depleted in iron relative to Earth's, but this result is highly influenced by radius measurement currently discrepant between Spitzer and TESS to 4σ .

We recommend in-depth transit spectroscopy with JWST to characterize the atmosphere on LHS 1140 b which we predict would create a CO₂ feature at 4.3 μ m, potentially as small as \sim 15 ppm according to self-consistent 3D global climate modeling of the planet in

the water world hypothesis. These simulations show that the atmospheric CO_2 concentration controls the surface temperature and the extent of a liquid water ocean. For an Earth-like case (1 bar N_2 , 400 ppm CO_2), liquid water is limited to a small patch at the substellar point, while for a CO_2 -dominated atmosphere (5 bar CO_2), almost a whole hemisphere is covered. These future observations could reveal the first exoplanet with a potentially habitable atmosphere and surface.

We thank the anonymous referee for constructive comments and suggestions that improved the presentation of this letter.

This study uses public ESPRESSO data under program IDs 0102.C-0294(A), 0103.C-0219(A), and 0104.C-0316(A) (PI: J. Lillo-Box).

This work is partly supported by the Natural Science and Engineering Research Council of Canada and the Trottier Institute for Research on Exoplanets through the Trottier Family Foundation.

We acknowledge the use of public TESS Alert data from pipelines at the TESS Science Office and at the TESS Science Processing Operations Center. Resources supporting this work were provided by the NASA High-End Computing (HEC) Program through the NASA Advanced Supercomputing (NAS) Division at Ames Research Center for the production of the SPOC data products. This letter includes data collected by the TESS mission that are publicly available from the Mikulski Archive for Space Telescopes (MAST).

This work has been carried out within the framework of the NCCR PlanetS supported by the Swiss National Science Foundation (SNSF) under grants 51NF40_182901 and 51NF40_205606. This project has received funding from the SNSF for project 200021_200726. F.P. would like to acknowledge the SNSF for supporting research with ESPRESSO and NIRPS through grants nr. 140649, 152721, 166227, 184618 and 215190.

This project has received funding from the European Research Council (ERC) under the European Union's Horizon 2020 research and innovation program (grant agreement SCORE No 851555)

Co-funded by the European Union (ERC, FIERCE, 101052347). Views and opinions expressed are however those of the author(s) only and do not necessarily reflect those of the European Union or the European Research Council. Neither the European Union nor the granting authority can be held responsible for them.

M.T. thanks the Gruber Foundation for its generous support to this research, support from the Trem-

plin 2022 program of the Faculty of Science and Engineering of Sorbonne University, and the Generic PCM team for the teamwork development and improvement of the model. This work was performed using the High-Performance Computing (HPC) resources of Centre Informatique National de l'Enseignement Supérieur (CINES) under the allocations No. A0100110391 and A0120110391 made by Grand Équipement National de Calcul Intensif (GENCI).

T.J.F. acknowledges support from the GSFC Sellers Exoplanet Environments Collaboration (SEEC), which is funded in part by the NASA Planetary Science Divisions Internal Scientist Funding Model.

R.A. is a Trottier Postdoctoral Fellow and acknowledges support from the Trottier Family Foundation. This work was supported in part through a grant from the Fonds de Recherche du Québec - Nature et Technologies (FRQNT).

J.I.G.H., V.M.P., and A.S.M. acknowledge financial support from the Spanish Ministry of Science and Innovation (MICINN) project PID2020-117493GB-I00 and A.S.M. from the Government of the Canary Islands project ProID2020010129.

This work was supported by Fundação para a Ciência e a Tecnologia (FCT) through national funds and by FEDER through COMPETE2020 - Programa Operacional Competitividade e Internacionalização by these grants: UIDB/04434/2020; UIDP/04434/2020. The research leading to these results has received fund-

ing from the European Research Council through the grant agreement 101052347 (FIERCE). E.D.M. acknowledges the support from through Stimulus FCT contract 2021.01294.CEECIND and by the following grants: UIDB/04434/2020 & UIDP/04434/2020 and 2022.04416.PTDC.

B.L.C.M. and J.R.M. acknowledge continuous grants from the Brazilian funding agencies CNPq and Print/CAPES/UFRN. This study was financed in part by the Coordenação de Aperfeiçoamento de Pessoal de Nível Superior - Brasil (CAPES) - Finance Code 001.

T.H. acknowledges support from an NSERC Alexander Graham Bell CGS-D scholarship.

X.D. acknowledges support by the French National Research Agency in the framework of the Investissements d'Avenir program (ANR-15-IDEX-02), through the funding of the "Origin of Life" project of the Grenoble-Alpes University.

Facilities: Spitzer, HST, TESS, ESO-VLT/ESPRESSO, ESO-La Silla/NIRPS

Software: emcee (Foreman-Mackey et al. 2013); Astropy (Astropy Collaboration et al. 2018); radvel (Fulton et al. 2018); matplotlib (Hunter 2007); juliet (Espinoza et al. 2019); batman (Kreidberg 2015); SciPy (Virtanen et al. 2020); NumPy (Harris et al. 2020) zeus (Karamanis et al. 2021); seaborn (Waskom 2021); exofile (github.com/AntoineDarveau/exofile); corner (Foreman-Mackey 2016); PSG (Villanueva et al. 2022)

REFERENCES

Adibekyan, V., Dorn, C., Sousa, S. G., et al. 2021, Science, 374, 330, doi: 10.1126/science.abg8794

Agol, E., Dorn, C., Grimm, S. L., et al. 2021, Planet. Sci. J., 2, 1, doi: 10.3847/PSJ/abd022

Aguichine, A., Mousis, O., Deleuil, M., & Marcq, E. 2021, ApJ, 914, 84, doi: 10.3847/1538-4357/abfa99

Ahumada, R., Prieto, C. A., Almeida, A., et al. 2020, ApJS, 249, 3, doi: 10.3847/1538-4365/ab929e

Akeson, R. L., Chen, X., Ciardi, D., et al. 2013, PASP, 125, 989, doi: 10.1086/672273

Albert, L., Lafrenière, D., Doyon, R., et al. 2023, Publications of the Astronomical Society of the Pacific, 135, 075001, doi: 10.1088/1538-3873/acd7a3

Allard, F., Homeier, D., & Freytag, B. 2012, Philosophical Transactions of the Royal Society of London Series A, 370, 2765, doi: 10.1098/rsta.2011.0269

Allart, R., Lovis, C., Faria, J., et al. 2022, A&A, 666, A196, doi: 10.1051/0004-6361/202243629 Ambikasaran, S., Foreman-Mackey, D., Greengard, L., Hogg, D. W., & O'Neil, M. 2015, IEEE Transactions on Pattern Analysis and Machine Intelligence, 38, 252, doi: 10.1109/TPAMI.2015.2448083

Anglada-Escudé, G., & Butler, R. P. 2012, ApJS, 200, 15, doi: 10.1088/0067-0049/200/2/15

Anglada-Escudé, G., Amado, P. J., Barnes, J., et al. 2016, Nature, 536, 437, doi: 10.1038/nature19106

Artigau, É., Cadieux, C., Cook, N. J., et al. 2022, AJ, 164, 84, doi: 10.3847/1538-3881/ac7ce6

Asplund, M., Amarsi, A. M., & Grevesse, N. 2021, A&A, 653, A141, doi: 10.1051/0004-6361/202140445

Astropy Collaboration, Price-Whelan, A. M., Sipőcz, B. M., et al. 2018, AJ, 156, 123, doi: 10.3847/1538-3881/aabc4f

Astudillo-Defru, N., Díaz, R. F., Bonfils, X., et al. 2017, A&A, 605, L11, doi: 10.1051/0004-6361/201731581

Batalha, N. E., Mandell, A., Pontoppidan, K., et al. 2017, PASP, 129, 064501, doi: 10.1088/1538-3873/aa65b0

- Bell, T. J., Dang, L., Cowan, N. B., et al. 2021, MNRAS, 504, 3316, doi: 10.1093/mnras/stab1027
- Benedict, G. F., Henry, T. J., Franz, O. G., et al. 2016, AJ, 152, 141, doi: 10.3847/0004-6256/152/5/141
- Benneke, B., & Seager, S. 2013, ApJ, 778, 153, doi: 10.1088/0004-637X/778/2/153
- Bensby, T., Feltzing, S., & Lundström, I. 2003, A&A, 410, 527, doi: 10.1051/0004-6361:20031213
- Bertaux, J. L., Lallement, R., Ferron, S., Boonne, C., & Bodichon, R. 2014, Astronomy & Astrophysics, 564, A46, doi: 10.1051/0004-6361/201322383
- Binney, J., & Tremaine, S. 2008, Galactic Dynamics: Second Edition
- Blanco-Cuaresma, S. 2019, MNRAS, 486, 2075, doi: 10.1093/mnras/stz549
- Bland-Hawthorn, J., & Gerhard, O. 2016, ARA&A, 54, 529, doi: 10.1146/annurev-astro-081915-023441
- Böker, T., Beck, T. L., Birkmann, S. M., et al. 2023, PASP, 135, 038001, doi: 10.1088/1538-3873/acb846
- Bond, J. C., O'Brien, D. P., & Lauretta, D. S. 2010, ApJ, 715, 1050, doi: 10.1088/0004-637X/715/2/1050
- Bonsor, A., Jofré, P., Shorttle, O., et al. 2021, MNRAS, 503, 1877, doi: 10.1093/mnras/stab370
- Bouchy, F., Pepe, F., & Queloz, D. 2001, A&A, 374, 733, doi: 10.1051/0004-6361:20010730
- Bouchy, F., Doyon, R., Artigau, É., et al. 2017, The Messenger, 169, 21, doi: 10.18727/0722-6691/5034
- Boutle, I. A., Mayne, N. J., Drummond, B., et al. 2017, A&A, 601, A120, doi: 10.1051/0004-6361/201630020
- Cadieux, C., Doyon, R., Plotnykov, M., et al. 2022, AJ, 164, 96, doi: 10.3847/1538-3881/ac7cea
- Carter, P. J., Leinhardt, Z. M., Elliott, T., Walter, M. J., & Stewart, S. T. 2015, ApJ, 813, 72, doi: 10.1088/0004-637X/813/1/72
- Charnay, B., Blain, D., Bézard, B., et al. 2021, A&A, 646, A171, doi: 10.1051/0004-6361/202039525
- Charnay, B., Meadows, V., Misra, A., Leconte, J., & Arney, G. 2015, ApJL, 813, L1, doi: 10.1088/2041-8205/813/1/L1
- Cherubim, C., Cloutier, R., Charbonneau, D., et al. 2023, AJ, 165, 167, doi: 10.3847/1538-3881/acbdfd
- Cloutier, R., Doyon, R., Bouchy, F., & Hébrard, G. 2018, AJ, 156, 82, doi: 10.3847/1538-3881/aacea9
- Cloutier, R., & Menou, K. 2020, AJ, 159, 211, doi: 10.3847/1538-3881/ab8237
- Cook, N. J., Artigau, É., Doyon, R., et al. 2022, PASP, 134, 114509, doi: 10.1088/1538-3873/ac9e74
- Coulombe, L.-P., Benneke, B., Challener, R., et al. 2023, Nature, 620, 292, doi: 10.1038/s41586-023-06230-1

- Dang, L., Cowan, N. B., Schwartz, J. C., et al. 2018, Nature Astronomy, 2, 220, doi: 10.1038/s41550-017-0351-6
- Dawson, R. I., & Johnson, J. A. 2012, ApJ, 756, 122, doi: 10.1088/0004-637X/756/2/122
- Del Genio, A. D., Brain, D., Noack, L., & Schaefer, L. 2018, arXiv e-prints, arXiv:1807.04776. https://arxiv.org/abs/1807.04776
- Del Genio, A. D., Way, M. J., Amundsen, D. S., et al. 2019, Astrobiology, 19, 99, doi: 10.1089/ast.2017.1760
- Delmotte, N., Dolensky, M., Padovani, P., et al. 2006, in Astronomical Society of the Pacific Conference Series, Vol. 351, Astronomical Data Analysis Software and Systems XV, ed. C. Gabriel, C. Arviset, D. Ponz, & S. Enrique, 690
- Deming, D., Knutson, H., Kammer, J., et al. 2015, ApJ, 805, 132, doi: 10.1088/0004-637X/805/2/132
- Diamond-Lowe, H., Berta-Thompson, Z., Charbonneau, D., Dittmann, J., & Kempton, E. M. R. 2020, AJ, 160, 27, doi: 10.3847/1538-3881/ab935f
- Dittmann, J. A., Irwin, J. M., Charbonneau, D., et al. 2017, Nature, 544, 333, doi: 10.1038/nature22055
- Donati, J. F., Kouach, D., Moutou, C., et al. 2020, MNRAS, 498, 5684, doi: 10.1093/mnras/staa2569
- Dorn, C., Hinkel, N. R., & Venturini, J. 2017, A&A, 597, A38, doi: 10.1051/0004-6361/201628749
- Doyon, R., Willott, C. J., Hutchings, J. B., et al. 2023, PASP, 135, 098001, doi: 10.1088/1538-3873/acd41b
- Dumusque, X. 2018, A&A, 620, A47, doi: 10.1051/0004-6361/201833795
- Edwards, B., Changeat, Q., Mori, M., et al. 2021, AJ, 161, 44, doi: 10.3847/1538-3881/abc6a5
- Espinoza, N. 2018, Research Notes of the American Astronomical Society, 2, 209, doi: 10.3847/2515-5172/aaef38
- Espinoza, N., Kossakowski, D., & Brahm, R. 2019, MNRAS, 490, 2262, doi: 10.1093/mnras/stz2688
- Faria, J. P., Suárez Mascareño, A., Figueira, P., et al. 2022, A&A, 658, A115, doi: 10.1051/0004-6361/202142337
- Fauchez, T. J., Turbet, M., Villanueva, G. L., et al. 2019, ApJ, 887, 194, doi: 10.3847/1538-4357/ab5862
- Fazio, G. G., Hora, J. L., Allen, L. E., et al. 2004, ApJS, 154, 10, doi: 10.1086/422843
- Foreman-Mackey, D. 2016, The Journal of Open Source Software, 1, 24, doi: 10.21105/joss.00024
- Foreman-Mackey, D., Hogg, D. W., Lang, D., & Goodman, J. 2013, PASP, 125, 306, doi: 10.1086/670067
- Forget, F., & Leconte, J. 2014, Philosophical Transactions of the Royal Society of London Series A, 372, 20130084, doi: 10.1098/rsta.2013.0084

- Fulton, B. J., Petigura, E. A., Blunt, S., & Sinukoff, E. 2018, PASP, 130, 044504, doi: 10.1088/1538-3873/aaaaa8
- Fulton, B. J., Petigura, E. A., Howard, A. W., et al. 2017, AJ, 154, 109, doi: 10.3847/1538-3881/aa80eb
- Gaia Collaboration, Brown, A. G. A., Vallenari, A., et al. 2021, A&A, 649, A1, doi: 10.1051/0004-6361/202039657
- Gaia Collaboration, Vallenari, A., Brown, A. G. A., et al. 2023, A&A, 674, A1, doi: 10.1051/0004-6361/202243940
- Gan, T., Cadieux, C., Jahandar, F., et al. 2023, AJ, 166, 165, doi: 10.3847/1538-3881/acf56d
- Gardner, J. P., Mather, J. C., Abbott, R., et al. 2023, PASP, 135, 068001, doi: 10.1088/1538-3873/acd1b5
- Gillon, M., Triaud, A. H. M. J., Demory, B.-O., et al. 2017, Nature, 542, 456, doi: 10.1038/nature21360
- Ginzburg, S., Schlichting, H. E., & Sari, R. 2016, ApJ, 825, 29, doi: 10.3847/0004-637X/825/1/29
- —. 2018, MNRAS, 476, 759, doi: 10.1093/mnras/sty290
- Guillot, T., & Morel, P. 1995, A&AS, 109, 109
- Hallatt, T., & Wiegert, P. 2020, AJ, 159, 147, doi: 10.3847/1538-3881/ab7336
- Harris, C. R., Millman, K. J., van der Walt, S. J., et al. 2020, Nature, 585, 357, doi: 10.1038/s41586-020-2649-2
- Hawkins, K., Jofré, P., Masseron, T., & Gilmore, G. 2015, MNRAS, 453, 758, doi: 10.1093/mnras/stv1586
- Haywood, R. D., Collier Cameron, A., Queloz, D., et al. 2014, MNRAS, 443, 2517, doi: 10.1093/mnras/stu1320
- Hemley, R. J., Jephcoat, A. P., Mao, H. K., et al. 1987, Nature, 330, 737, doi: 10.1038/330737a0
- Higson, E., Handley, W., Hobson, M., & Lasenby, A. 2019, Statistics and Computing, 29, 891, doi: 10.1007/s11222-018-9844-0
- Hunter, J. D. 2007, Computing in Science and Engineering, 9, 90, doi: 10.1109/MCSE.2007.55
- Husser, T. O., Wende-von Berg, S., Dreizler, S., et al. 2013, A&A, 553, A6, doi: 10.1051/0004-6361/201219058
- Inamdar, N. K., & Schlichting, H. E. 2016, ApJL, 817, L13, doi: 10.3847/2041-8205/817/2/L13
- Irwin, J., Charbonneau, D., Nutzman, P., & Falco, E. 2009,
 in Transiting Planets, ed. F. Pont, D. Sasselov, & M. J.
 Holman, Vol. 253, 37–43,
 doi: 10.1017/S1743921308026215
- Jahandar, F., Doyon, R., Artigau, É., et al. 2023, arXiv e-prints, arXiv:2310.12125, doi: 10.48550/arXiv.2310.12125
- Jenkins, J. M., Twicken, J. D., McCauliff, S., et al. 2016, in Society of Photo-Optical Instrumentation Engineers (SPIE) Conference Series, Vol. 9913, Software and Cyberinfrastructure for Astronomy IV, ed. G. Chiozzi & J. C. Guzman, 99133E, doi: 10.1117/12.2233418

- Karamanis, M., Beutler, F., & Peacock, J. A. 2021, MNRAS, 508, 3589, doi: 10.1093/mnras/stab2867
- Kipping, D. M. 2010, MNRAS, 407, 301, doi: 10.1111/j.1365-2966.2010.16894.x
- —. 2013, MNRAS, 435, 2152, doi: 10.1093/mnras/stt1435
- —. 2014, MNRAS, 440, 2164, doi: 10.1093/mnras/stu318
- Kite, E. S., & Ford, E. B. 2018, ApJ, 864, 75, doi: 10.3847/1538-4357/aad6e0
- Kordopatis, G., Schultheis, M., McMillan, P. J., et al. 2023, A&A, 669, A104, doi: 10.1051/0004-6361/202244283
- Kreidberg, L. 2015, PASP, 127, 1161, doi: 10.1086/683602
- Leconte, J., Wu, H., Menou, K., & Murray, N. 2015, Science, 347, 632, doi: 10.1126/science.1258686
- Lee, E. J., & Connors, N. J. 2021, ApJ, 908, 32, doi: 10.3847/1538-4357/abd6c7
- Li, C., & Zhao, G. 2017, ApJ, 850, 25, doi: 10.3847/1538-4357/aa93f4
- Lillo-Box, J., Figueira, P., Leleu, A., et al. 2020, A&A, 642, A121, doi: 10.1051/0004-6361/202038922
- Lindegren, L. 2018.
 - http://www.rssd.esa.int/doc_fetch.php?id=3757412
- Luque, R., & Pallé, E. 2022, Science, 377, 1211, doi: 10.1126/science.abl7164
- Madhusudhan, N., Piette, A. A. A., & Constantinou, S. 2021, ApJ, 918, 1, doi: 10.3847/1538-4357/abfd9c
- Madhusudhan, N., Sarkar, S., Constantinou, S., et al. 2023, ApJL, 956, L13, doi: 10.3847/2041-8213/acf577
- Majewski, S. R., APOGEE Team, & APOGEE-2 Team. 2016, Astronomische Nachrichten, 337, 863, doi: 10.1002/asna.201612387
- Mann, A. W., Feiden, G. A., Gaidos, E., Boyajian, T., & von Braun, K. 2015, ApJ, 804, 64, doi: 10.1088/0004-637X/804/1/64
- Mann, A. W., Dupuy, T., Kraus, A. L., et al. 2019, ApJ, 871, 63, doi: 10.3847/1538-4357/aaf3bc
- Marounina, N., & Rogers, L. A. 2020, ApJ, 890, 107, doi: 10.3847/1538-4357/ab68e4
- Ment, K., Dittmann, J. A., Astudillo-Defru, N., et al. 2019, AJ, 157, 32, doi: 10.3847/1538-3881/aaf1b1
- Morrison, R. A., Jackson, J. M., Sturhahn, W., Zhang, D., & Greenberg, E. 2018, Journal of Geophysical Research (Solid Earth), 123, 4647, doi: 10.1029/2017JB015343
- Owen, J. E., & Wu, Y. 2017, ApJ, 847, 29, doi: 10.3847/1538-4357/aa890a
- Patel, J. A., & Espinoza, N. 2022, AJ, 163, 228, doi: 10.3847/1538-3881/ac5f55
- Pepe, F., Mayor, M., Rupprecht, G., et al. 2002, The Messenger, 110, 9. https:
 - //ui.adsabs.harvard.edu/2002Msngr.110....9P/abstract

- Pepe, F., Cristiani, S., Rebolo, R., et al. 2021, A&A, 645, A96, doi: 10.1051/0004-6361/202038306
- Piaulet, C., Benneke, B., Almenara, J. M., et al. 2023,Nature Astronomy, 7, 206,doi: 10.1038/s41550-022-01835-4
- Plotnykov, A., & Valencia, D. 2020, MNRAS, 499, 932
- Rajpaul, V., Aigrain, S., Osborne, M. A., Reece, S., & Roberts, S. 2015, MNRAS, 452, 2269, doi: 10.1093/mnras/stv1428
- Reddy, B. E., Lambert, D. L., & Allende Prieto, C. 2006, MNRAS, 367, 1329,
 - doi: 10.1111/j.1365-2966.2006.10148.x
- Reylé, C., Jardine, K., Fouqué, P., et al. 2021, A&A, 650, A201, doi: 10.1051/0004-6361/202140985
- Reylé, C., Jardine, K., Fouqué, P., et al. 2022, in Cambridge Workshop on Cool Stars, Stellar Systems, and the Sun, Cambridge Workshop on Cool Stars, Stellar Systems, and the Sun, 218, doi: 10.5281/zenodo.7669746
- Ribas, I., Bolmont, E., Selsis, F., et al. 2016, A&A, 596, A111, doi: 10.1051/0004-6361/201629576
- Ricker, G. R., Winn, J. N., Vanderspek, R., et al. 2015, Journal of Astronomical Telescopes, Instruments, and Systems, 1, 014003, doi: 10.1117/1.JATIS.1.1.014003
- Rogers, J. G., Schlichting, H. E., & Owen, J. E. 2023, ApJL, 947, L19, doi: 10.3847/2041-8213/acc86f
- Rogers, L. A. 2015, ApJ, 801, 41, doi: 10.1088/0004-637X/801/1/41
- Sabotta, S., Schlecker, M., Chaturvedi, P., et al. 2021, A&A, 653, A114, doi: 10.1051/0004-6361/202140968
- Scora, J., Valencia, D., Morbidelli, A., & Jacobson, S. 2020, MNRAS, 493, 4910, doi: 10.1093/mnras/staa568
- Seager, S., & Mallén-Ornelas, G. 2003, ApJ, 585, 1038, doi: 10.1086/346105
- Silva, A. M., Faria, J. P., Santos, N. C., et al. 2022, A&A, 663, A143, doi: 10.1051/0004-6361/202142262
- Skrutskie, M. F., Cutri, R. M., Stiening, R., et al. 2006, AJ, 131, 1163, doi: 10.1086/498708
- Smith, J. C., Stumpe, M. C., Van Cleve, J. E., et al. 2012, PASP, 124, 1000, doi: 10.1086/667697
- Spaargaren, R. J., Wang, H. S., Mojzsis, S. J., Ballmer,
 M. D., & Tackley, P. J. 2023, ApJ, 948, 53,
 doi: 10.3847/1538-4357/acac7d
- Speagle, J. S. 2020, MNRAS, 493, 3132, doi: 10.1093/mnras/staa278
- Stewart, S. T., & Ahrens, T. J. 2005, Journal of Geophysical Research (Planets), 110, E03005, doi: 10.1029/2004JE002305
- Stixrude, L., & Lithgow-Bertelloni, C. 2011, Geophysical Journal International, 184, 1180, doi: 10.1111/j.1365-246X.2010.04890.x

- Stock, S., Kemmer, J., Kossakowski, D., et al. 2023, A&A, 674, A108, doi: 10.1051/0004-6361/202244629
- Stumpe, M. C., Smith, J. C., Catanzarite, J. H., et al. 2014, PASP, 126, 100, doi: 10.1086/674989
- Stumpe, M. C., Smith, J. C., Van Cleve, J. E., et al. 2012, PASP, 124, 985, doi: 10.1086/667698
- Suárez Mascareño, A., González-Álvarez, E., Zapatero Osorio, M. R., et al. 2023, A&A, 670, A5, doi: 10.1051/0004-6361/202244991
- Thiabaud, A., Marboeuf, U., Alibert, Y., Leya, I., & Mezger, K. 2015, A&A, 580, A30, doi: 10.1051/0004-6361/201525963
- Trotta, R. 2008, Contemporary Physics, 49, 71, doi: 10.1080/00107510802066753
- Tsiaras, A., Waldmann, I. P., Rocchetto, M., et al. 2016, ApJ, 832, 202, doi: 10.3847/0004-637X/832/2/202
- Turbet, M., Bolmont, E., Ehrenreich, D., et al. 2020, A&A, 638, A41, doi: 10.1051/0004-6361/201937151
- Turbet, M., Leconte, J., Selsis, F., et al. 2016, A&A, 596, A112, doi: 10.1051/0004-6361/201629577
- Turbet, M., Bolmont, E., Leconte, J., et al. 2018, A&A, 612, A86, doi: 10.1051/0004-6361/201731620
- Turbet, M., Fauchez, T. J., Leconte, J., et al. 2023, arXiv e-prints, arXiv:2308.15110, doi: 10.48550/arXiv.2308.15110
- Unterborn, C. T., Dismukes, E. E., & Panero, W. R. 2016, ApJ, 819, 32, doi: 10.3847/0004-637X/819/1/32
- Valencia, D., Guillot, T., Parmentier, V., & Freedman, R. S. 2013, ApJ, 775, 10, doi: 10.1088/0004-637X/775/1/10
- Valencia, D., Sasselov, D. D., & O'Connell, R. J. 2007, ApJ, 656, 545, doi: 10.1086/509800
- Van Eylen, V., & Albrecht, S. 2015, ApJ, 808, 126, doi: 10.1088/0004-637X/808/2/126
- Villanueva, G. L., Liuzzi, G., Faggi, S., et al. 2022, Fundamentals of the Planetary Spectrum Generator
- Villanueva, G. L., Smith, M. D., Protopapa, S., Faggi, S., & Mandell, A. M. 2018, JQSRT, 217, 86, doi: 10.1016/j.jqsrt.2018.05.023
- Virtanen, P., Gommers, R., Oliphant, T. E., et al. 2020, Nature Methods, 17, 261, doi: 10.1038/s41592-019-0686-2
- Wagner, W., & Pruß, A. 2002, Journal of Physical and Chemical Reference Data, 31, 387, doi: 10.1063/1.1461829
- Waskom, M. 2021, The Journal of Open Source Software, 6, 3021, doi: 10.21105/joss.03021
- Wildi, F., Bouchy, F., Doyon, R., et al. 2022, in Society of Photo-Optical Instrumentation Engineers (SPIE)
 Conference Series, Vol. 12184, Ground-based and Airborne Instrumentation for Astronomy IX, ed. C. J.
 Evans, J. J. Bryant, & K. Motohara, 121841H,

doi: 10.1117/12.2630016

Wolf, E. T., Shields, A. L., Kopparapu, R. K., Haqq-Misra, J., & Toon, O. B. 2017, ApJ, 837, 107, doi: 10.3847/1538-4357/aa5ffc

Wordsworth, R. D., Forget, F., Selsis, F., et al. 2011, ApJL, 733, L48, doi: 10.1088/2041-8205/733/2/L48

Yang, J., Ji, W., & Zeng, Y. 2020, Nature Astronomy, 4, 58, doi: 10.1038/s41550-019-0883-z

Zechmeister, M., Reiners, A., Amado, P. J., et al. 2018, A&A, 609, A12, doi: 10.1051/0004-6361/201731483

APPENDIX

A. LIGHT CURVES

In this appendix, we present the light curves of LHS 1140 from *Spitzer*, HST, and TESS. The four individual transits of LHS 1140 b and one of LHS 1140 c acquired with *Spitzer* are presented in Figure A1. The single transit visit from HST with the Wide Field Camera 3 (white light curve) is shown in Figure A2. Lastly, the full TESS light curves from Sectors 3 and 30 are presented in Figure A3.

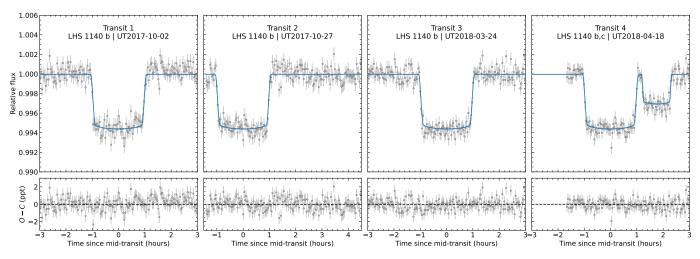


Figure A1. Individual *Spitzer* transits of LHS 1140 b (Transit 1–4) and c (Transit 4 only). The best-fit transit models of the planets are shown in blue with the residual of this fit shown below.

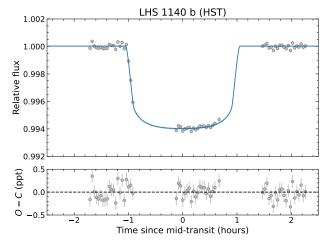


Figure A2. White light curve transit of LHS 1140 b with the Wide Field Camera 3 on HST. The best-fit transit model is shown in blue with the residuals of this fit shown on the bottom panel.

B. RADIAL VELOCITY MEASUREMENTS

The ESPRESSO radial velocity of LHS 1140 extracted with the line-by-line method are shown in Figure B1 and listed in Table B1 fully available online.

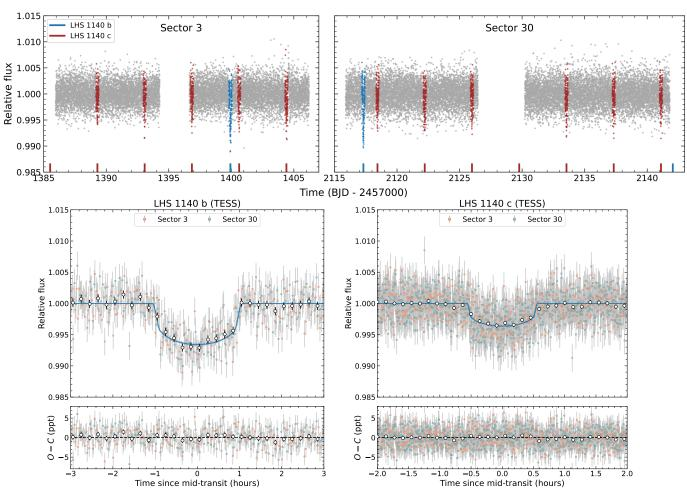


Figure A3. Top panels: Normalized PDCSAP light curve of LHS 1140 from TESS Sectors 3 and 30. The blue and red vertical ticks and data points highlight the transits of planet b and c. Bottom panels: Phase-folded transit of LHS 1140 b (left) and c (right). The open circles represent the binned photometry, respectively 12- and 8-minute bins for b and c. The best-fit transit models are depicted with blue curves. The residuals of the fits are shown below their respective transit.

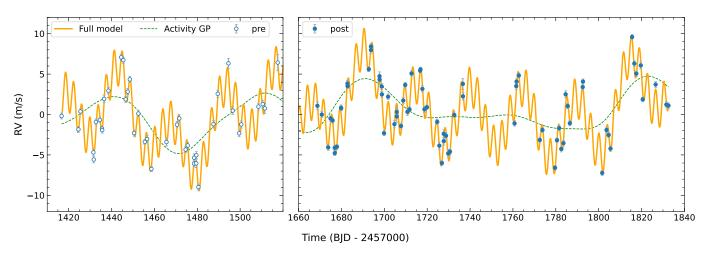


Figure B1. Radial velocity time series of LHS 1140 with ESPRESSO produced with the line-by-line method. The data before (pre) and after (post) the fiber upgrade of ESPRESSO (June 2019) are distinguished with open and solid circles, respectively. The full RV model (planet b, planet c, and activity GP) is represented by an orange curve, with the activity GP component highlighted with a green dashed curve (details in Appendix D.1).

Table B1. ESPRESSO radial velocity of LHS 1140 obtained with the line-by-line method

BJD - 2400000	$RV (m s^{-1})$	$\sigma_{\rm RV}~({\rm ms}^{-1})$
58416.711656	-13457.505	0.364
58424.576752	-13459.164	0.360
58425.528804	-13456.943	0.343
58431.527205	-13462.007	0.453
58431.714392	-13462.893	0.423
58432.733559	-13458.241	0.383
58434.555946	-13457.993	0.346

Note—Table B1 is published in its entirety in machine-readable format.

C. SUPPLEMENTARY MATERIAL OF THE STELLAR CHARACTERIZATION

C.1. Stellar age

We analysed the kinematics of LHS 1140 to characterize its age. This was done by assessing whether the star belongs to the Galaxy's thin or thick disk stellar populations; thick disk stars are older (\sim 10 Gyr) than their counterparts in the thin disk, have different chemistry ([Fe/H] \sim -0.5, [α /Fe] \sim +0.3; Reddy et al. 2006), and are kinematically hotter, with larger velocity dispersions relative to the Local Standard of Rest (LSR), and larger orbital excursions from the Galactic midplane (Binney & Tremaine 2008). We employed the astrometric solution from Gaia DR3 (Gaia Collaboration et al. 2023). We note that the solution's renormalized unit weight error ruwe=1.53 indicates that there is some uncertainty in the astrometry (ruwe \lesssim 1.4 for well-behaved solutions; Lindegren 2018). The orbit of LHS 1140 was integrated forward in time 60 Myr using the Monte Carlo model outlined in Hallatt & Wiegert (2020).

These calculations produce a velocity with respect to the Local Standard of Rest $(U_{\rm LSR}, V_{\rm LSR}, W_{\rm LSR}) = (14.38 \pm 0.041, -38.52 \pm 0.09, 11.18 \pm 0.41)~{\rm km\,s^{-1}}$, yielding $V_{\rm tot} = \sqrt{U_{\rm LSR}^2 + V_{\rm LSR}^2 + W_{\rm LSR}^2} = 42.61 \pm 0.20~{\rm km\,s^{-1}}$ (adopting the Local Standard of Rest from Bland-Hawthorn & Gerhard 2016). This places LHS 1140 in the thin disk, where $V_{\rm tot,thin} \lesssim 50~{\rm km\,s^{-1}}$ (e.g., Bensby et al. 2003; Hawkins et al. 2015). Its orbital oscillation amplitude above/below the Galactic midplane is $131 \pm 5~{\rm pc}$, significantly smaller than that of thick disk stars (~1 kpc; e.g., Li & Zhao 2017) and consistent with that of thin disk stars ~a few Gyr old (see Fig. 20 of Kordopatis et al. 2023). This result for the age of LHS 1140 is consistent with D17 (>5 Gyr) estimated from its slow rotation period and absence of H α emission. We thus adopt that LHS 1140 has a relatively old age >5 Gyr and is a thin disk star.

C.2. Bayesian inference of stellar mass and radius from transits

Measured directly from transit light curves, the orbital period (P) and the scaled semi-major axis (a/R_{\star}) of an exoplanet allow the determination of the density of its host star (Seager & Mallén-Ornelas 2003):

$$\rho_{\star,\text{transit}} = \frac{3\pi}{GP^2} \left(\frac{a}{R_{\star}}\right)^3 \tag{C1}$$

While Equation C1 is fundamentally true for all orbits, as it is essentially a reformulation of Kepler's Third Law (with G the gravitational constant), the a/R_{\star} inferred from transit can be significantly biased when assuming a circular orbit (e.g., Kipping 2010, Dawson & Johnson 2012, Kipping 2014). Following the notation of Van Eylen & Albrecht (2015), the true stellar density (ρ_{\star}) when photo-eccentric effects are considered is given by:

$$\frac{\rho_{\star}}{\rho_{\star,\text{transit}}} = \frac{\left(1 - e^2\right)^{3/2}}{\left(1 + e\sin\omega\right)^3} \tag{C2}$$

where e and ω are respectively the orbital eccentricity and argument of periastron of the transiting planet. Unaccounted eccentricity as small as $e \sim 0.1$ can potentially induce a 30% error in ρ_{\star} . From our joint transit RV analysis

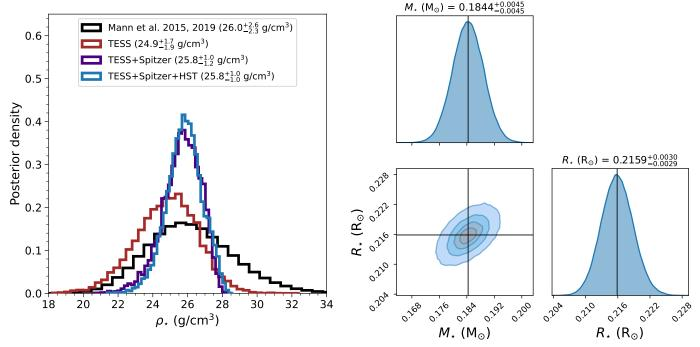


Figure C1. Left panel: Stellar density (ρ_{\star}) distribution of LHS 1140 using mass and radius from Mann et al. 2015, 2019 (black) and posterior distributions of ρ_{\star} inferred from TESS (red), TESS+Spitzer (purple), and TESS+Spitzer+HST (blue) transits. Right panel: Bayesian inference of the stellar mass and radius of LHS 1140 using the TESS+Spitzer+HST constraints on ρ_{\star} as a measurement and Mann et al. (2015, 2019) as a prior. The positive covariance in M_{\star} - R_{\star} space indicates that both parameters are likely to vary in the same direction to produce a constant ρ_{\star} constrained by the transits.

(Appendix D.1), we measure $\rho_{\star}/\rho_{\star, \rm transit}$ of 1.00 ± 0.03 for LHS 1140 b and 1.02 ± 0.04 for LHS 1140 c consistent with perfectly circular orbits ($e_{\rm b} < 0.043$, $e_{\rm c} < 0.050$ with 95% confidence). As both orbital solutions satisfy $\rho_{\star} \approx \rho_{\star, \rm transit}$, we hereafter drop the transit subscript when referring to stellar density obtained from our transit light curves. As summarized in Figure C1, our measurement of ρ_{\star} constrained by Spitzer, HST, and TESS has resulted in new posteriors for the mass and radius of the star LHS 1140, namely $M_{\star} = 0.1844 \pm 0.0045 \, {\rm M}_{\odot}$ and $R_{\star} = 0.2159 \pm 0.0030 \, {\rm R}_{\odot}$. This Bayesian approach is taken to improve the precision on M_{\star} and R_{\star} , otherwise the dominant sources of uncertainty for the inferred planetary mass and radius.

C.3. Additional Tables and Figure

We recapitulate the stellar parameters of LHS 1140 in Table C1. After, we present the stellar abundance determination from NIRPS (Sect. 3.2) in Table C2 and give corresponding chemical weight ratios in Table C3. An example of this chemical spectroscopy analysis for the Al I line (1675.514 nm) is presented in Figure C2.

D. DATA ANALYSIS

D.1. Joint transit RV fit

The joint analysis of the photometric (*Spitzer*, HST, and TESS) and RV (ESPRESSO) data is done with juliet (Espinoza 2018), an all-in-one package that combines transit and RV modeling using batman (Kreidberg 2015) and radvel (Fulton et al. 2018) with multiple sampling options (e.g., Markov Chain Monte Carlo, nested sampling). Here, we select the dynesty (Speagle 2020) sampler in juliet for parameter estimations and Bayesian log-evidence (ln Z) calculations relevant for model comparisons. The dynesty package implements dynamic nested sampling algorithms (Higson et al. 2019) designed for more efficient and robust estimations of complex posterior distributions. We follow

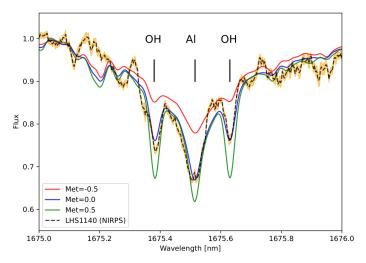


Figure C2. NIRPS template spectrum of LHS 1140 (black dashed line) around the Al I line (1675.514 nm). The orange envelope depicts the flux dispersion measured on 29 individual observations. Three ACES models with a fixed $T_{\rm eff} = 3100 \, \rm K$ and metallicities of -0.5 (red line), 0.0 (blue line) and 0.5 dex (green line) are shown. For this single line, we measure [Al/H] = $0.0 \pm 0.1 \, \rm dex$. This figure illustrates the precision of the NIRPS data to constrain elemental abundances often different from that of iron ([Fe/H] = $-0.15 \pm 0.09 \, \rm dex$).

Table C1. LHS 1140 stellar parameters

Parameter	Value	Ref.			
Astrometry	and kinematics				
RA (J2016.0)	00:44:59.33	1			
DEC (J2016.0)	-15:16:17.54	1			
$\mu_{\alpha}\cos\delta \; (\mathrm{mas}\cdot\mathrm{yr}^{-1})$	318.152 ± 0.049	1			
$\mu_{\delta} \; (\text{mas} \cdot \text{yr}^{-1})$	-596.623 ± 0.054	1			
$\pi \text{ (mas)}$	66.8287 ± 0.0479	1			
d (pc)	14.9636 ± 0.0107	1			
$U (\mathrm{km s}^{-1})$	14.38 ± 0.041	2			
$V (\mathrm{km} \mathrm{s}^{-1})$	-38.52 ± 0.09	2			
$W (\mathrm{km} \mathrm{s}^{-1})$	11.18 ± 0.41	2			
Physical	Physical parameters				
$M_{\star}~({ m M}_{\odot})$	0.1844 ± 0.0045	2			
$R_{\star} \; (\mathrm{R}_{\odot})$	0.2159 ± 0.0030	2			
$\rho_{\star} \; (\mathrm{g \cdot cm^{-3}})$	25.8 ± 1.0	3			
$T_{\rm eff}$ (K)	3096 ± 48	2			
$L_{\star} \; (\mathrm{L}_{\odot})$	0.0038 ± 0.0003	3			
SpT	M4.5V	4			
[Fe/H] (dex)	-0.15 ± 0.09	2			
$\log g \text{ (cgs)}$	5.041 ± 0.016	3			
Age	$> 5\mathrm{Gyr}$	4			
$P_{\rm rot}$ (days)	131 ± 5	4			

References—(1) Gaia DR3 (Gaia Collaboration et al. 2021). (2) This work. (3) This work derived from M_{\star} , R_{\star} , and $T_{\rm eff}$ (4) Dittmann et al. (2017).

Table C2. LHS 1140 stellar abundances measured with NIRPS for various chemical species with important features in the near-infrared

Element	[X/H]	σ	# of lines
Fe I	-0.15	0.09	3
Al I	0.00	0.10	2
Mg I	0.11	0.10	2
Si I	-0.20	0.10	1
Ca I	0.20	0.10	1
OI^*	0.00	0.01	82
CI	0.10	0.10	3
<> [†]	0.01	0.04	_

NOTE—*The oxygen abundance is inferred from OH lines. $^\dagger Average$ abundance of all elements.

Table C3. LHS 1140 stellar abundance weight ratios*

Ratios	LHS 1140	Sun^{\dagger}	$M dwarf^{\ddagger}$
Fe/Mg [w]	$1.03^{+0.40}_{-0.29}$	1.87 ± 0.22	[0.89, 2.92]
Mg/Si[w]	$1.94^{+0.79}_{-0.56}$	0.95 ± 0.09	[0.69, 1.66]
Fe/O[w]	$0.15^{+0.04}_{-0.03}$	0.21 ± 0.03	[0.08, 0.28]
C/O [w]	$0.56^{+0.17}_{-0.13}$	0.44 ± 0.06	[0.21, 0.60]

NOTE—*Weight ratios calculated using X/Y [w] = $10^{A(X)}/10^{A(Y)} \times (m_{\rm X}/m_{\rm Y})$ with $A({\rm X}) = [{\rm X/H}] + A_{\rm solar}({\rm X})$ the absolute logarithmic abundance, $A_{\rm solar}({\rm X})$ taken from Table 2 of Asplund et al. (2021), and $m_{\rm X}$ the atomic mass of element X.

the dynesty documentation⁶ and choose the random slice sampling option since the number of free parameters exceeds 20.

The orbit of planet k (k: 'b', 'c', 'd') is described by four parameters, the orbital period P_k , the time of inferior conjunction $t_{0,k}$, the eccentricity e_k , and the argument of periastron ω_k , and one systemic parameter, the stellar density ρ_{\star} , common for all planets. For multi-planetary systems, a single ρ_{\star} exists, which eliminates the need to fit semi-major axes (a_k/R_{\star}) for each planet (Equation C1). We define a Gaussian prior on the stellar density of LHS 1140 based on Mann et al. (2015, 2019): $\rho_{\star} \sim \mathcal{N}\left(26.0, 2.6^2\right) \text{g cm}^{-3}$. For the transiting planets b and c, we follow the Espinoza et al. (2019) transformation of the transit impact parameter b and planet-to-star radius ratio $p = R_p/R_{\star}$ into r_1 and r_2 parameters to only sample physically plausible regions in b-p space. We model the baseline flux of the Spitzer, HST, and TESS light curves with the parameter M described in Espinoza (2018) and include per-instrument extra jitter terms (σ_{Spitzer} , σ_{HST} , and σ_{TESS}).

Synthetic spectra of M dwarfs often show significant discrepancy with the observations (Blanco-Cuaresma 2019), implying that theoretical limb-darkening (LD) predictions may be unreliable. Patel & Espinoza (2022) have found systematic offsets between empirical quadratic LD coefficients (u_1,u_2) and theoretical predictions in the TESS bandpass of the order $\Delta u_1, \Delta u_2 \approx 0.2$ for cool stars similar to LHS 1140. Differing from previous transit analyses (D17; M19; LB20; Edwards et al. 2021), we do not fix or apply Gaussian priors on the LD coefficients, but let them vary freely (uniform priors). The stellar LD effects in the *Spitzer*, HST, and TESS transits are modeled using per-instrument quadratic q_1 and q_2 parameters (Kipping 2013) constructed to only allow physical solutions for values between 0 and

[†]Solar weight ratios from Asplund et al. (2021).

[‡]95% confidence interval of the M dwarf population (~1000) of APOGEE DR16 (Majewski et al. 2016; Ahumada et al. 2020)

⁶ dynesty.readthedocs.io/en/stable/index.html

1. Note fixing the LD parameters to those measured by previous studies for the same instrument does not change the median of our $R_{\rm p}/R_{\star}$ posteriors.

For the Keplerian component, a semi-amplitude K_k for each planet is fitted, as well as instrumental RV offsets $(\gamma_{\text{pre}}, \gamma_{\text{post}})$ and extra white noise terms $(\sigma_{\text{pre}}, \sigma_{\text{post}})$ for ESPRESSO pre- and post-fiber upgrade. When testing for possible eccentric orbits, we sample uniformly $\sqrt{e_k} \cos \omega_k$ and $\sqrt{e_k} \sin \omega_k$ between -1 and 1. We include in juliet a Gaussian Process (GP) to model stellar activity in the ESPRESSO RVs. Our GP implementation in juliet runs george (Ambikasaran et al. 2015) with a quasi-periodic covariance kernel (Haywood et al. 2014; Rajpaul et al. 2015):

$$k_{i,j} = A^2 \exp\left[-\frac{|t_i - t_j|^2}{2\ell^2} - \Gamma \sin^2\left(\frac{\pi|t_i - t_j|}{P_{\text{rot}}}\right)\right]$$
(D3)

where $|t_i - t_j|$ is the time interval between data i and j, A is the amplitude of the GP, ℓ is the coherence timescale, Γ scales the periodic component of the GP, and P_{rot} is the stellar rotation period. We adopt a Gaussian prior on the known rotation period of the star $P_{\text{rot}} \sim \mathcal{N}\left(131,5^2\right)$ days. The priors for the other GP hyperparameters are listed in Table D2 and mostly follow the recommendation of Stock et al. 2023 (GP Prior III) when the rotation period is already constrained.

We inspected three different joint models (\mathcal{M}) :

- Two planets, LHS 1140 b and c, on circular orbits (\mathcal{M}_{2cp} ; $e_b = e_c = 0$, $\omega_b = \omega_c = 90^\circ$)
- Two planets, LHS 1140 b and c, on eccentric orbits (\mathcal{M}_{2ep})
- Three planets, LHS 1140 b, c, and the candidate planet d reported by LB20, on circular orbits (\mathcal{M}_{3cp} ; $e_b = e_c = e_d = 0$, $\omega_b = \omega_c = \omega_d = 90^\circ$)

The difference in Bayesian log-evidence ($\Delta \ln Z$) yields the probability that one model describes better the observations over another. The empirical scale of Trotta 2008 (see Table 1 therein) serves to interpret the significance of $\Delta \ln Z$ and to select the "best" model. A $\Delta \ln Z > 5$ constitutes "strong" evidence in favour of the model with the highest $\ln Z$. A $2.5 < \Delta \ln Z < 5$ corresponds to "moderate" evidence, but a $\Delta \ln Z \leq 2.5$ means that neither model should be favoured. Multiple runs of each $\mathcal M$ were carried with dynesty to verify the consistency of $\ln Z$.

For the two planet models $\mathcal{M}_{2\mathrm{cp}}$ and $\mathcal{M}_{2\mathrm{ep}}$, we obtain a $\Delta \ln Z = 0.8 \pm 0.9$ in favour of the circular orbit solutions (inconclusive). We report from model $\mathcal{M}_{2\mathrm{ep}}$ upper limits on e_{b} and e_{c} (95% confidence) of 0.043 and 0.050, respectively, implying that in all likelihood, the orbit of LHS 1140 b and c are de facto circular. For this reason, we select the simpler $\mathcal{M}_{2\mathrm{cp}}$ as the preferred model. We present the relevant planetary parameters derived from the joint transit RV fit for model $\mathcal{M}_{2\mathrm{cp}}$ in Table D1. The priors and posteriors (16th, 50th, and 84th percentiles) of the free parameters of model $\mathcal{M}_{2\mathrm{cp}}$ are reported in Table D2. The best-fit transit models of the *Spitzer*, HST, and TESS light curves are respectively shown in Figures 1, A2, and A3. The phase-folded RVs with the best-fit orbital solutions of LHS 1140 b and c is shown in Figure 2 with the full RV model (Keplerian + activity GP) presented in Figure B1. This full RV model yields a residual RMS of 41 cm s⁻¹ for the "pre" data consistent with the median RV errors of 42 cm s⁻¹. For the "post" data, the residual dispersion of 54 cm s⁻¹ is larger than the typical RV errors of 34 cm s⁻¹ so that a $\sigma_{\mathrm{post}} = 36 \pm 6$ cm s⁻¹ jitter term is needed to fully describe the scatter.

The reanalysis of the ESPRESSO data with the LBL framework is an opportunity to test the presence of the candidate LHS 1140 d on a 78.9-day orbit reported by LB20. For model \mathcal{M}_{3cp} , we chose the same priors on $P_{\rm d}$, $t_{0,\rm d}$, and $K_{\rm d}$ as in LB20, namely \mathcal{U} (70, 120) days, \mathcal{U} (2458350, 2458400) BJD, and \mathcal{U} (0, 10) m s⁻¹. This fit converges to a small semi-amplitude of $0.9^{+0.8}_{-0.6}$ m s⁻¹ and an undefined period of 87^{+14}_{-9} days for a planet d. The Bayesian log-evidence does not increase when adding a third planet with $\Delta \ln Z = -1.0 \pm 0.9$ between \mathcal{M}_{3cp} and \mathcal{M}_{2cp} . We also reject a $K_{\rm d}$ larger than 2.21 m s⁻¹ at 2σ , corresponding to the median signal detected in LB20. LHS 1140 could realistically have other planets, but given the precision of our RV measurements, we see no evidence of an additional companion sharing the parameters of candidate LHS 1140 d. In Appendix D.3, we further demonstrate that an 80-day RV signal is most likely of stellar origin.

D.2. Transit depth discrepancy for LHS 1140 c

In LB20, the radius of LHS 1140 b and c measured by TESS was slightly smaller (by 1.5σ and 2σ respectively) compared with previous results by M19 obtained with *Spitzer* (see Fig. 3). Here, our joint analysis of *Spitzer*, HST (for LHS 1140 b only), and TESS data has resulted in a similar discrepancy for planet c, but not for b. In Figure D1, we

Table D1.	Planetary parameters	derived from	the joint	transit RV fit
-----------	----------------------	--------------	-----------	----------------

Parameter	LHS 1140 b	LHS $1140\mathrm{c}$	Description			
	Orbital parameters					
P (days)	24.73723 ± 0.00002	3.777940 ± 0.000002	Period			
$t_0 \text{ (BJD - } 2457000)$	1399.9300 ± 0.0003	1389.2939 ± 0.0002	Time of inferior conjunction			
a (au)	0.0946 ± 0.0017	0.0270 ± 0.0005	Semi-major axis			
$i \ (^{\circ})$	89.86 ± 0.04	$89.80^{+0.14}_{-0.19}$	Inclination			
e	< 0.043 (95%)	< 0.050 (95%)	Eccentricity			
	Tran	sit parameters				
b	$0.23^{+0.05}_{-0.07}$	$0.09^{+0.09}_{-0.06}$	Impact parameter			
$\delta \; (\mathrm{ppt})$	5.38 ± 0.06	2.90 ± 0.09	Depth			
t_{14} (hours)	2.15 ± 0.05	1.13 ± 0.02	Duration			
	Physical parameters					
$R_{\rm p}~({ m R}_{\oplus})$	1.730 ± 0.025	1.272 ± 0.026	Radius			
$M_{ m p}~({ m M}_{\oplus})$	5.60 ± 0.19	1.91 ± 0.06	Mass			
$\rho \; (\mathrm{g \cdot cm^{-3}})$	5.9 ± 0.3	5.1 ± 0.4	Bulk density			
$S (S_{\oplus})$	0.43 ± 0.03	5.3 ± 0.4	Insolation			
$T_{\rm eq} [A_{\rm B} = 0] (K)$	226 ± 4	422 ± 7	Equilibrium temperature			

show the transit impact parameter (b) and scaled radius ($p = R_p/R_{\star}$) of LHS 1140 b and c derived from fitting each instrument independently. The b-p posteriors of LHS 1140 b agree well for all available instruments, but we detect a 4σ tension for the p of LHS 1140 c measured by *Spitzer* and TESS.

We remain cautious before interpreting the transit depth discrepancy of LHS 1140 c as real because we only have a single visit with Spitzer. It is possible that data reduction systematics affected the depth measurement. Nonetheless, it is worth mentioning that Spitzer Channel 2 at 4.5 μ m covers a strong CO_2 feature. We detect a difference of 500 ppm between the Spitzer and TESS bandpasses, meaning that if excess atmospheric absorption is causing this discrepancy, it would be readily detectable with JWST. This work calls for better radius determination for LHS 1140 c, particularly obtaining the full near-infrared transmission spectrum of this planet with JWST to reveal its true radius that we currently report as an average between Spitzer and TESS (see Joint in Fig. D1) and test whether its atmosphere is CO_2 -rich.

D.3. Validating genuine Keplerian signals with line-by-line radial velocity

The LBL method allows to verify the achromaticity of the inferred semi-amplitudes of the LHS 1140 planets. The three-planet model $\mathcal{M}_{3\mathrm{cp}}$ can be applied on velocities derived per spectral bins of $\Delta\lambda \approx 20\,\mathrm{nm}$ in the entire ESPRESSO domain. For genuine Keplerian signals:

- (chromaticity test) the K_{λ} calculated for different bands are achromatic, i.e., $dK_{\lambda}/d\lambda = 0$.
- (coherence test) the K_{λ} add constructively (coherent period and phase), yielding a consistent weighted average (value and uncertainty) with K resulting from the full spectral range.
- (noise test) the semi-amplitude uncertainties (σ_K) should scale with RV precision (σ_{RV}) according to the Cloutier et al. (2018) formalism, i.e., $\sigma_K = \sigma_{RV} \sqrt{2/N_{RV}}$ when no important extra jitter is detected.

These three criteria can be tested for LHS 1140 b, c, and the non-transiting candidate d. As summarized in Figure D2, we measure no chromaticity for the Keplerian signals of LHS 1140 b and c, respectively with $dK_{\lambda}/d\lambda = 0.11 \pm 0.10$ and $0.03 \pm 0.08 \text{ m s}^{-1}$ per 100 nm. For the candidate LHS 1140 d, the signal is marginally larger in the blue wavelengths of ESPRESSO ($dK_{\lambda}/d\lambda = -0.42 \pm 0.26 \text{ m s}^{-1}$ per 100 nm). Similarly, since the Doppler signals of LHS 1140 b and c are perfectly coherent, the weighted average of the K_{λ} are consistent with the K obtained from the full spectral range (see Fig. D2). This is not observed for the 80-day signal associated with candidate d for which fitting a Keplerian model on

Table D2. Prior and posterior distributions of the joint transit RV fit

Parameter	Prior ¹	Posterior	Description
Stellar parameter			
$\rho_{\star} \; (\mathrm{g \cdot cm^{-3}})$	$\mathcal{N}\left(26.0, 2.6^2\right)$	25.8 ± 1.0	Stellar density
LHS 1140 b			
$P_{\rm b}$ (days)	U(24.7, 24.8)	24.73723 ± 0.00002	Orbital period
$t_{0,b}$ (BJD - 2457000)	\mathcal{U} (1399.9, 1400.0)	1399.9300 ± 0.0003	Time of inferior conjunction
$r_{ m 1,b}$	$\mathcal{U}\left(0,1 ight)$	0.49 ± 0.03	Parameterization ² for b and p
$r_{2,\mathrm{b}}$	$\mathcal{U}\left(0,1 ight)$	0.0733 ± 0.0004	Parameterization ² for b and p
$K_{\rm b}~({\rm ms^{-1}})$	$\mathcal{U}\left(0,10 ight)$	3.80 ± 0.11	RV semi-amplitude
LHS 1140 c			
$P_{\rm c}$ (days)	U(3.7, 3.8)	3.777940 ± 0.000002	Orbital period
t _{0,c} (BJD - 2457000)	U (1389.25, 1389.35)	1389.2939 ± 0.0002	Time of inferior conjunction
$r_{1,c}$	$\mathcal{U}\left(0,1 ight)$	0.39 ± 0.05	Parameterization ² for b and p
$r_{ m 2,c}$	$\mathcal{U}(0,1)$	0.0539 ± 0.0008	Parameterization ² for b and p
$K_{\rm c}~({\rm ms^{-1}})$	$\mathcal{U}\left(0,10\right)$	2.42 ± 0.07	RV semi-amplitude
Photometric parameters	,		
$q_{1,\mathrm{Spitzer}}$	$\mathcal{U}\left(0,1\right)$	$0.016^{+0.018}_{-0.009}$	Limb-darkening parameter ³
$q_{2,\mathrm{Spitzer}}$	$\mathcal{U}(0,1)$	$0.42^{+0.36}_{-0.28}$	Limb-darkening parameter ³
$M_{\rm Spitzer}$ (ppm)	$\mathcal{N}(0, 1000^2)$	34 ± 23	Baseline flux
$\sigma_{ m Spitzer}$ (ppm)	$\mathcal{L}\mathcal{U}(1, 1000)$	15^{+57}_{-12}	Extra white noise
$q_{1,\mathrm{HST}}$	$\mathcal{U}(0,1)$	0.28 ± 0.08	Limb-darkening parameter ³
$q_{2,\mathrm{HST}}$	$\mathcal{U}(0,1)$	$0.12^{+0.11}_{-0.08}$	Limb-darkening parameter ³
M_{HST} (ppm)	$\mathcal{N}(0, 1000^2)$	-25 ± 22	Baseline flux
$\sigma_{ m HST} \ (m ppm)$	$\mathcal{L}\mathcal{U}(1, 1000)$	12^{+38}_{-10}	Extra white noise
$q_{1,\mathrm{TESS}}$	$\mathcal{U}(0,1)$	$0.33^{+0.20}_{-0.12}$	Limb-darkening parameter ³
$q_{2,\mathrm{TESS}}$	$\mathcal{U}(0,1)$	0.56 ± 0.27	Limb-darkening parameter ³
$M_{\rm TESS}$ (ppm)	$\mathcal{N}\left(0,1000^2\right)$	9 ± 48	Baseline flux
σ_{TESS} (ppm)	$\mathcal{L}\mathcal{U}(1, 1000)$	17^{+116}_{-14}	Extra white noise
$RV\ parameters$			
$\gamma_{\rm pre}~({ m ms}^{-1})$	$\mathcal{U}(-10, 10)$	1.3 ± 1.5	$\mathrm{RV}\ \mathrm{offset}^4$
$\gamma_{\rm post} ({\rm ms}^{-1})$	U(-10, 10)	-0.6 ± 1.4	$\mathrm{RV}\ \mathrm{offset}^4$
$\sigma_{\rm pre}~({\rm ms^{-1}})$	$\mathcal{L}\mathcal{U}(10^{-3}, 10)$	$0.04^{+0.18}_{-0.03}$	Extra white noise
$\sigma_{\rm post} \ ({\rm ms}^{-1})$	$\mathcal{L}\mathcal{U}\left(10^{-3},10\right)$	0.36 ± 0.06	Extra white noise
RV activity GP			
$A \text{ (m s}^{-1})$	$\mathcal{L}U$ (10 ⁻³ , 10)	$2.8_{-0.6}^{+1.0}$	Amplitude of the GP
$\ell \text{ (days)}$	$\mathcal{L}\mathcal{U}$ (100, 1000)	164^{+62}_{-42}	Timescale of the GP
Γ	$\mathcal{L}\mathcal{U}\left(0.1,10\right)$	$3.7^{+1.5}_{-1.2}$	Periodic scale of the GP
$P_{\rm rot}$ (days)	$\mathcal{N}\left(131,5^2\right)$	133 ± 3	Rotation period

NOTE— ${}^1\mathcal{U}(a,b)$ is the uniform distribution between value a and b, $\mathcal{L}\mathcal{U}(a,b)$ is the log-uniform (Jeffreys) distribution between value a and b, $\mathcal{N}(\mu,\sigma^2)$ is the normal distribution with mean μ and variance σ^2 . 2 Parameterization of the transit impact parameter (b) and the planet-to-star radius ratio $(p = R_p/R_\star)$ outlined in Espinoza (2018).

 $^{^{3}}q_{1},q_{2}$ are related to the quadratic limb-darkening coefficients u_{1},u_{2} by the transformations described in Kipping (2013).

⁴Relative to the median RV (-13458.5 and -13450.5 m s⁻¹ for pre- and post-fiber change data).

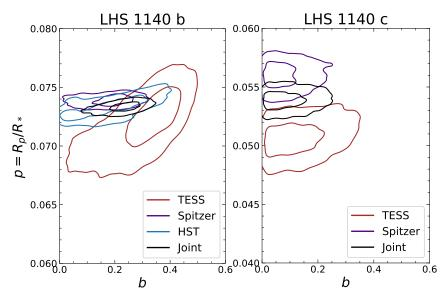


Figure D1. Posterior distributions (1 and 2σ contours) for the transit impact parameter (b) and scaled radius ($p = R_p/R_{\star}$) of LHS 1140 b and c. Different colors refer to fit on TESS (red), *Spitzer* (purple), and HST (blue) data only. The black contours are the final joint posteriors on all available instruments. A $\sim 4\sigma$ tension in p exists between *Spitzer* and TESS for LHS 1140 c.

RVs derived from the full ESPRESSO wavelength range is three times less accurate. Finally, given the RV precision of this data set varying from 4.73 to $0.65~{\rm m\,s^{-1}}$ in the $450-750\,{\rm nm}$ interval, we find that LHS 1140 b and c follow the Cloutier et al. (2018) formalism, but not d (see Fig. D2, right). Interestingly, the spectral interval $700-725\,{\rm nm}$ covering only 8% of the ESPRESSO domain contains 30% of all the RV content of LHS 1140. The tests presented in this section provide evidence against the existence of LHS $1140\,{\rm d}$ first announced by LB20 as a candidate non-transiting planet.

E. SUPPLEMENTARY MATERIAL OF THE INTERNAL STRUCTURE ANALYSIS

E.1. Interior modeling

In this appendix, we summarize the method of Plotnykov & Valencia (2020) adapted to constrain the detailed internal structure of LHS 1140 b.

We used a Bayesian analysis with Markov Chain Monte Carlo (MCMC) sampling with emcee (Foreman-Mackey et al. 2013) coupled to the internal structure model of Valencia et al. (2007). The model assumes three layers for the interior of the planet: a condensed water (liquid/ice) layer at the surface, a mantle (Mg-Si rock) and a core (Fe-Ni-Si alloy). A fixed atmospheric layer is also considered for models in which the atmosphere could significantly contribute to the planet radius. The water layer is described by the equation of state (EOS) of Hemley et al. 1987; Wagner & Pruß 2002; Stewart & Ahrens 2005 and we adopt the density mixing model with EOS parameters of Stixrude & Lithgow-Bertelloni (2011) and Morrison et al. (2018) for the mantle and the core, respectively. The lower mantle is assumed to be composed of bridgmanite/post-perovskite and wustite (at different proportions to that of Earth), while the upper mantle is modeled as pure olivine (Mg₂SiO₄). This choice was made in light of the possible low Si content of the star that may indicate olivine formation is favoured compared to pyroxenes (Mg₂Si₂O₆).

Important ingredients to the model are the abundance ratios (by weight) of refractory elements, namely Fe/Mg and Mg/Si. We explored a no prior (Fe/Mg unconstrained) and a stellar prior (Fe/Mg following the star) models for the water world case of LHS 1140 b (Sect. 4.2.3). For the pure rocky case (Sect. 4.2.2), the planet Fe/Mg ratio must be lower than that of the host star to produce the observed density. Consequently, only the unconstrained Fe/Mg analysis was done. Note that because we model three layers for the interior, the no prior case cannot fully constrain both the CMF and WMF, i.e., planetary interior models are inherently degenerate in this case. For all models, the Mg/Si ratio in the mantle is assumed to be that of the host star: Mg/Si_{planet} $\sim \mathcal{N}(\text{Mg/Si}_{\text{star}}, \sigma_{\text{star}}^2)$. Despite LHS 1140 having a Mg/Si approximately twice that of the Sun/Earth (see Table C3), this ratio only weakly influences the final radius of the planet meaning that our results do not depend on the exact mineralogy of the rocks.

We report the posterior distributions of our interior analysis in Appendix E.2 for all interior models considered. Additionally, we compare the Fe/Mg distributions of LHS 1140 b for different scenarios in Figure E1.

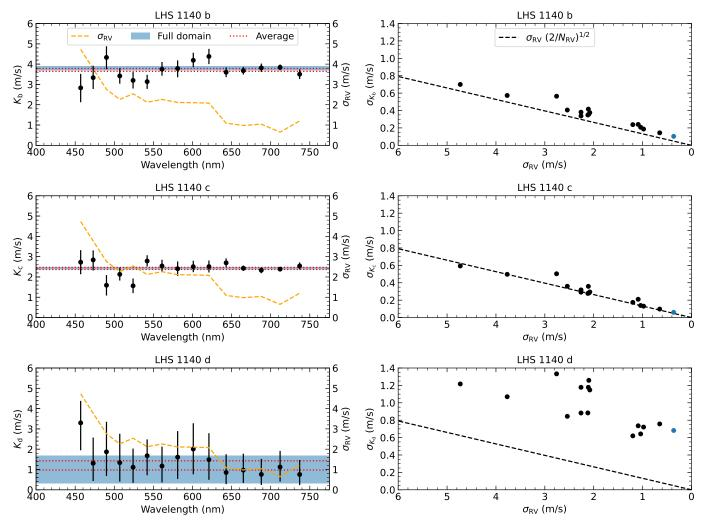


Figure D2. Validating Keplerian signals in the ESPRESSO spectral domain of LHS 1140. Left panels: Semi-amplitudes K_{λ} obtained with model $\mathcal{M}_{3\text{cp}}$ from LBL radial velocities extracted for different bands ($\Delta\lambda\approx20\,\mathrm{nm}$). The per-band velocities have uncertainties ($\sigma_{\rm RV}$) varying from 4.73 to 0.65 ms⁻¹ (orange dashed lines). A genuine Keplerian signal is achromatic ($dK_{\lambda}/d\lambda=0$). We measure no chromatic slopes for LHS 1140 b and c, but the signal of candidate LHS 1140 d is marginally larger in the blue wavelengths of ESPRESSO ($dK_{\lambda}/d\lambda=-0.42\pm0.26~\mathrm{m\,s^{-1}}$ per 100 nm). A coherent signal such as a Doppler shift affecting all wavelengths should produce consistent K between the full spectrum constraints (1σ confidence regions in blue) and the weighted average of the K_{λ} (1σ confidence interval between the red dotted lines). Assuming a coherent signal, the $K_{\rm d}$ inferred from the full ESPRESSO domain should have an uncertainty $\sigma_{K_{\rm d}}\sim0.18\,\mathrm{m\,s^{-1}}$, which is inconsistent with observations. Right panels: Semi-amplitude uncertainties σ_K with increasing RV precision (smaller $\sigma_{\rm RV}$). A coherent signal in wavelengths should follow the Cloutier et al. (2018) formalism ($\sigma_K=\sigma_{\rm RV}\sqrt{2/N_{\rm RV}}$), which is not seen for LHS 1140 d. The LBL data set shows no evidence of an 80-day signal associated with the candidate planet LHS 1140 d.

E.2. Posterior distributions

We summarize the posterior distributions of Fe/Mg for LHS 1140 b in Figure E1 for the pure rocky (Sect. 4.2.2) and water world (Sect. 4.2.3) scenarios. The posteriors from our MCMC sampling are also presented in the following corner plots of Figures E2, E3, and E4 showing the results for a bare rock, a water world (no prior, stellar prior, and solar prior cases), and a Hycean world, respectively.

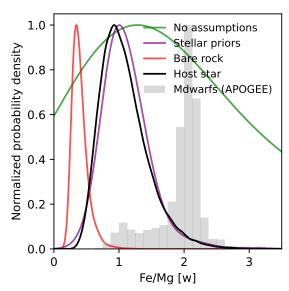


Figure E1. Fe/Mg distribution for LHS 1140 b according to different assumptions (no prior or stellar prior) for the bare rock (red) and water world (green and purple) models compared to the host star (black). We plot the kernel density estimate of the interior model posterior, which is normalized to have mode of 1. We include the M dwarfs distribution of Fe/Mg from the APOGEE DR16 (gray histogram, sample size of ~ 1000 ; Majewski et al. 2016; Ahumada et al. 2020) for comparison.

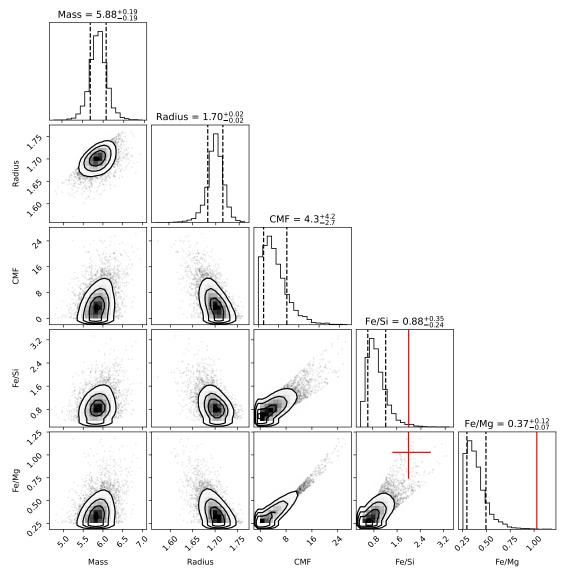


Figure E2. Posterior distribution for LHS 1140 b interior parameters for the bare rock scenario (WMF = 0). Chemical weight ratios Fe/Si and Fe/Mg are derived quantities. The red lines (and red cross) in Fe/Si and Fe/Mg space correspond to the stellar measurements. The vertical black dashed lines represent 16th and 84th percentiles of the posterior.

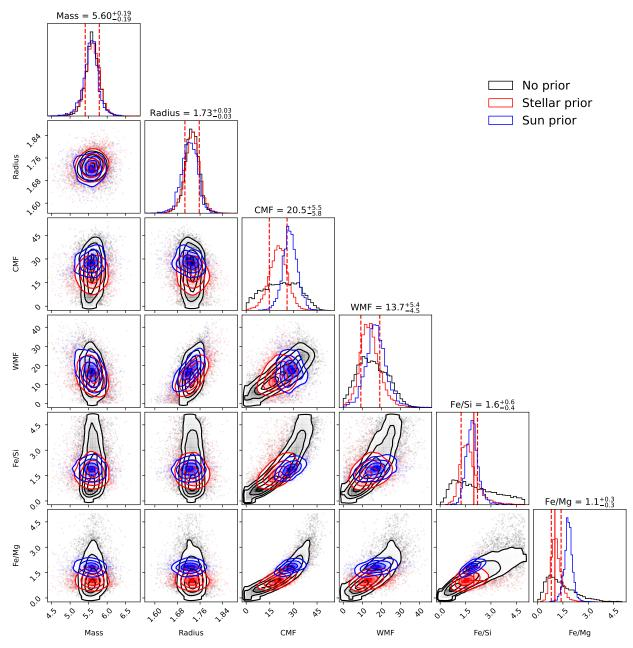


Figure E3. Posterior distribution for LHS 1140 b interior parameters for the water world scenario (WMF > 0) for different Fe/Mg assumptions: no prior (black), stellar prior (red) and Sun prior (blue). For the stellar and Sun prior cases, the log-probability function is modified to include the restriction posed by Fe/Mg and Mg/Si ratios measured on the host star or the Sun (Table C3). The red lines (and red cross) in Fe/Si and Fe/Mg space correspond to the stellar measurements. The vertical red dashed lines represent 16th and 84th percentiles of the posterior for the stellar prior case. Note the values in the parameter titles are for the stellar prior case only.

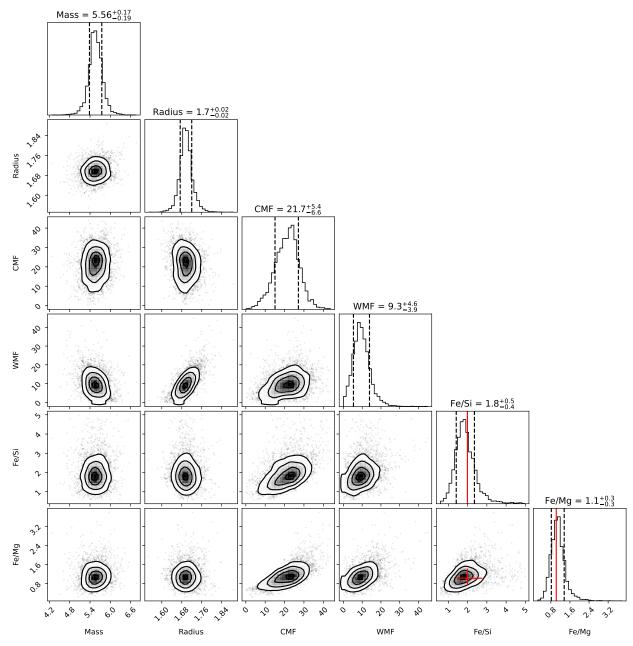


Figure E4. Posterior distribution for LHS 1140 b interior parameters for the Hycean world scenario (icy planet with 250 km $\rm H_2$ atmosphere on top). Here, we use the same assumptions as the stellar prior water world model. The red lines (and red cross) represent the stellar ratios, while the vertical black dashed lines are the 16th and 84th percentiles of the posterior. Note the simulation radius is smaller ($\Delta R_p \sim 0.03 R_{\oplus}$) due to $\rm H_2$ atmosphere which is not included in our interior model.